SATIF-15:
15th Workshop on Shielding aspects of Accelerators, Targets, and Irradiation Facilities

Facility for Rare Isotope Beams (FRIB) at Michigan State University
East Lansing, Michigan USA
20-23 September 2022.

Session 4: Code Benchmarking & Intercomparison

Table of contents

1. Machine Learning Based Scaling Model for Radiation Transport Calculations at FRIB

J.C. Zamora[1*], G. Bollen [1], T. Ginter [1], R. Ronningen[1], D. Georgobiani [2]
[1]Facility for Rare Isotope Beams, Michigan State University, East Lansing, Michigan 48824, USA
[2]Fermi National Accelerator Laboratory, Batavia, Illinois, USA
[*]email address: zamora@frib.msu.edu

A neural-network algorithm was trained with a large set of radiation-transport calculations to predict the dose rate produced by stopping ion beams in the range from ^{16}O to ^{208}Pb. The algorithm provides a global prediction for any beam particle and initial conditions, such as energy and beam power. The trained neural network was applied for scaling dose-rate maps and extrapolating to other beam conditions. The model represents a new method to obtain an approximate dose-rate map with relatively short computing time (a few seconds). The results are in fair agreement with real radiation transport calculations in most cases. A more complete model including the angular distribution of reaction products will be necessary in order to improve the prediction of the neural network at forward angles.

1.1. Introduction

The Facility for Rare Isotope Beams (FRIB) is a new U.S. national user facility located at Michigan State University, which started operations in the spring of 2022 (Castelvecchi, 2022). FRIB will enable precise measurements with the broadest range of rare isotopes of any existing facility, including many never-before-synthesized isotopes.

FRIB is designed to accelerate all stable ions, ranging from hydrogen to uranium, at energies up to and exceeding 200 MeV/u with a beam power on the production target of up to 400 kW. After in-flight fragment production and separation, the rare-isotope beams can also be stopped, or stopped and then reaccelerated. The fast, stopped, and reaccelerated rare-isotope beams are delivered to experimental areas where dedicated detector setups are employed to investigate the fundamental properties of nuclear matter.

Radiation transport (RT) calculations at FRIB are particularly challenging due to the large variety of experimental conditions (i.e., beam species, energy, power, shielding, etc.). Additionally, part of the facility is still under construction, making the possible scenarios that need to be supported by RT calculations even more complex.

Scaling models provide an efficient alternative to estimate the radiation level of a given scenario based on existing RT calculations. For example, the scaling method becomes relevant for extrapolating dose-rate maps to any beam isotope, energy, power, etc. In particular, this method reduces the time needed to provide an estimate from several hours to a few seconds. This work investigates the feasibility of using Machine Learning (ML) techniques for scaling RT calculations. The use of ML codes has become a very powerful method to extract information from very large data sets with multiple dimensions. Also, ML algorithms' adaptability and good performance offer an interesting alternative for RT applications.

1.2. Method

Traditional programming generally employs input data and a set of logical rules to obtain a predictive response. Unlike conventional programming, ML uses input and response data (called “training set”) to infer the logical rules of a program. The building blocks of a neural

network in ML are the neurons, inspired by the brain neural system that contains billions of neurons connected to form a network. These ML algorithms are composed of multiple layers of neurons that are fully connected. When data are propagated between layers, the response function of a node is given by a multiple linear regression (Bishop, 2006)

$$y = \sum_{i}^{m} w_i x_i + b,$$

where x_i is the input data, w_i is the weight that determines the importance of a neuron in a precedent layer, and b is the bias parameter that represents how far off the prediction is from the intended value. The connection between adjacent layers is composed of several of these operations that increase the level of abstraction of an algorithm. Both weights and biases are trainable parameters in the neural network and are adjusted to obtain the predicted best-fit output.

In this work, we have implemented an ML code for processing RT calculations for several beam isotopes and energies. The output of the code predicts the total dose rate for given input conditions. A sketch of the neural network code implemented in this work is shown in Figure 1.1. In between the input and output layers, fully-connected hidden layers were included to optimize the predictive model. We used the ReLU (rectified linear activation unit) function $[max(0, x)]$ to guarantee a minimum value at zero and to prevent gradient saturation (Bishop, 2006). The ReLU function is also a non-linear activation that helps the network learn a non-linear operation, as required in this study. The Loss function was defined as the mean-squared error, and the optimizer chosen was ADAM (Kingma and Ba, 2014). In total, 602,945 trainable parameters were used to learn the features of the RT calculations.

Figure 1.1. Sketch of the neural network implemented in this work. The input parameters are the beam energy, mass (*A*) and neutron (*N*) numbers. The output is the predicted dose rate

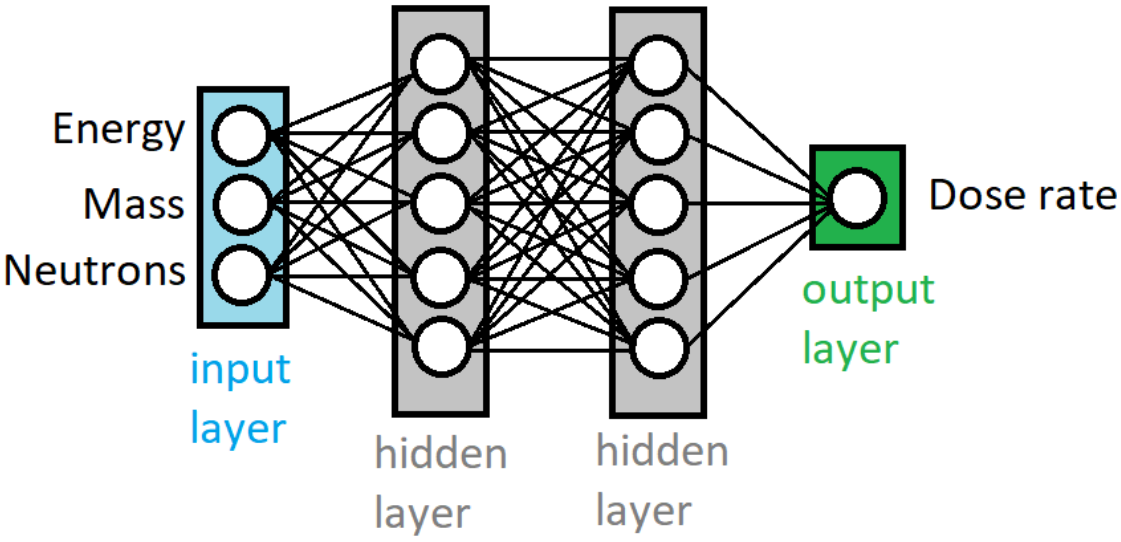

1.2.1. Creating the training data set

The training data set was created from a large number of RT calculations using the code PHITS (Sato et al., 2018). All the stable isotopes ranging from ^{16}O to ^{208}Pb (238 isotopes) were assumed as beam particles at energies from 50 to 400 MeV/u. The selection of these

beams covers almost the complete operation conditions of FRIB. The beam intensity was fixed at 1×10^9 pps (particles per second) for all the calculations. A target composed of natural copper and a thickness of 6 cm was assumed in order to stop completely any beam in the target. A spherical surface (1 m radius) centered at the target position was used as a scoring detector (air). An illustration of the simulated geometry is shown in Figure 1.2(left panel). All the reaction products generated by the interaction of the beam particles in the copper target were counted and transformed to an equivalent dose rate. In total, 1904 PHITS simulations were performed. Integrated dose-rate at 1 m and dose-rate maps were extracted for each calculation. Figure 1.2(right panel) shows an example of the dose-rate map for ^{208}Pb at 400 MeV/u. The training data set comprised 80% of the PHITS calculations randomly selected, while 20% were used for validation.

Figure 1.2. Radiation transport model used for creating the training data set

PHITS geometry (left panel). Example of dose rate map (arbitrary units) for ^{208}Pb at 400 MeV/u (right panel)

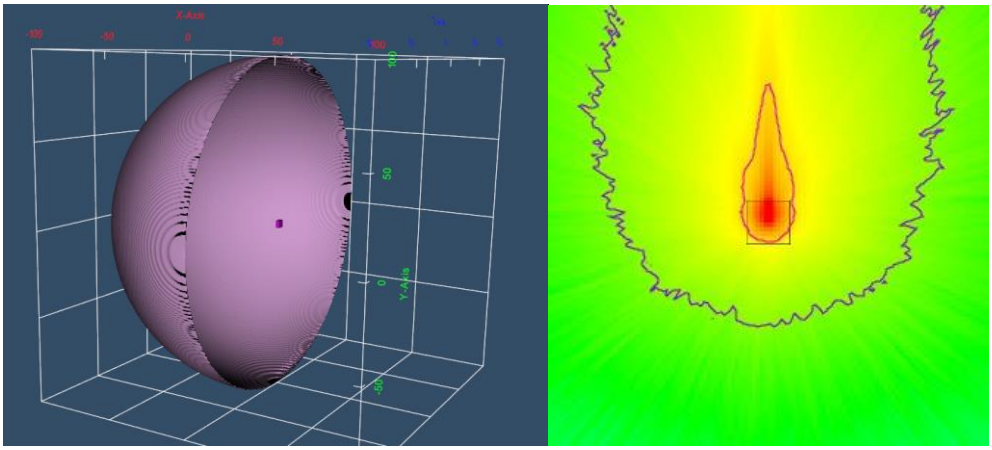

1.3. Neural-network prediction

Integrated dose rates as a function of the each beam energy (E_b), mass number (A), and neutron number (N) were used to train the neural network and provide a global prediction for any beam isotope and initial conditions. ML offers a powerful method to perform a multivariate regression and extract many features from raw data within the same model. For instance, Figures 1.3, 1.4, and 1.5 show the prediction for selected energies and masses as a function of $A^{1/3}$, N, and E_b, respectively. The data points correspond to the dose rate calculated with PHITS in arbitrary units. As seen in Figure 1.3, the data between $A^{1/3} = 2.5$ and 4 (which corresponds to beams ranging from ^{16}O and ^{63}Cu) are spread about ML predictions with differences up to 10%. However, the neural network provides an average dose-rate estimate that accounts for the global trend at any beam energy. For heavier nuclei, the dose rate increases almost linearly, and again, the neural network has successfully described the data. Figure 1.4 shows the dose rate as a function of the neutron number. Similarly, the dose rate from lighter nuclei are more dispersed, particularly at high energies. However, the ML prediction provides a consistent description of the data with a small sensitivity for outlier points. The dose rate for heavy mass nuclei, above ^{120}Sn, seems to have almost a linear dependency with the beam neutron number. Certainly, the slope of the linear component also depends on the beam energy, and the neural network is able to extract these types of features from the data. Finally, Figure 1.5 shows the data behavior as a function of the beam energy from selected beam mass regions: near ^{16}O ($A^{1/3} = 2.5$) and

near ^{166}Eu ($A^{1/3} = 5.5$). For all the cases, there is a clear quadratic dependency with the beam energy. The data provided to the neural network is comprised of only discrete beam energies from 50 to 400 MeV/u in steps of 50 MeV/u. However, the ML prediction also retrieves the information for other beam energies in the full range.

Our results are consistent with the semi-empirical formula of Kurosawa (Kurosawa et al. , 2000), which was obtained by fitting experimental data with beam particles ranging from helium to xenon having energies up to 800 MeV/u stopping in several target materials. This formula accounts for the integrated yield of neutrons with energies above 5 MeV and over a hemisphere from 0 to 90 degrees to the beam direction as:

$$Y = \frac{1.5 \times 10^{-6}}{N_t^{\frac{1}{3}}} E_b^2 \left(A_t^{1/3} + A_b^{1/3}\right)^2 N_b \frac{A_b}{Z_b^2} \quad (n/source),$$

where A, N, Z and E are the mass number, neutron number, charge number and energy, respectively. The indices b and t indicate a beam and a target isotope. A remarkable agreement with the E_b^2 and N_b dependency was also obtained with the neural network prediction. There is also a clear dependency on A_b, but the reconstructed distributions present a more complex behaviour than a simple power function.

Figure 1.3. PHITS calculations and the predicted dose rate as a function of $A^{1/3}$

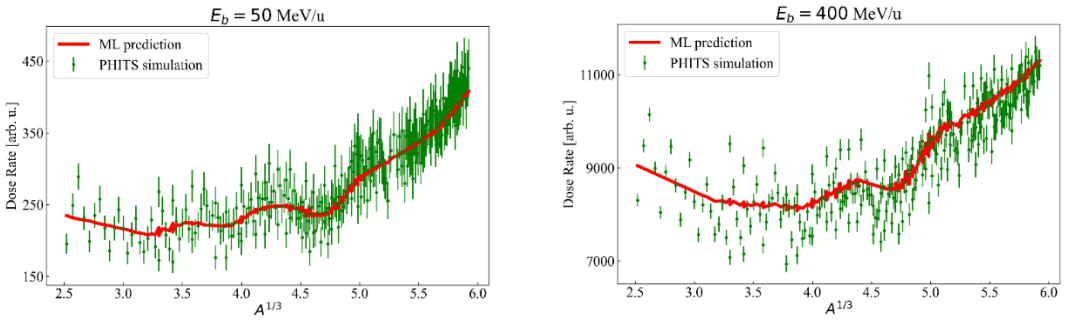

Figure 1.4. PHITS calculations and the predicted dose rate as a function of neutron number (*N*)

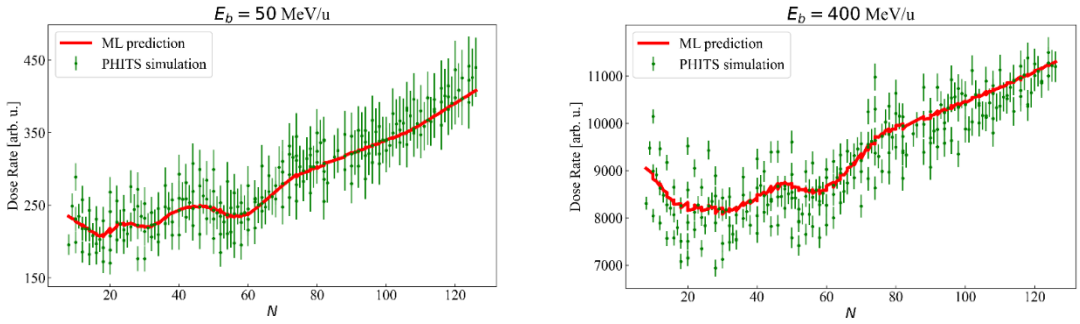

Figure 1.5. PHITS calculations and the predicted dose rate as a function of the beam energy (E_b)

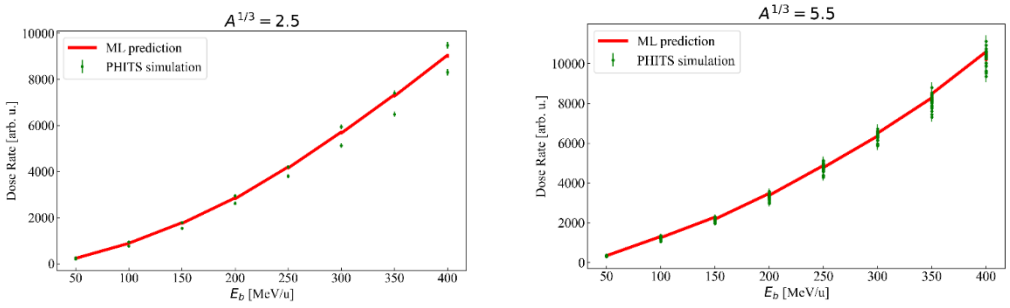

1.4. Application: scaling dose-rate maps

The main goal of training a neural network that predicts the integrated dose rate is to provide a fast method to obtain a conversion factor that transform an existing dose-rate map to another one with different initial conditions. For instance, this is quite useful for providing an educated guess of the dose rate for many beams and energies based on just one calculation. Certainly, this also reduces the computing time required for a radiation transport calculation from several hours to just a couple of seconds. In order to test the quality of the neural network prediction, we use a dose-rate map calculated with a ^{48}Ca beam, at 250 MeV/u and 1 kW, completely stopped in a copper target. This result can be used to extrapolate the dose rate with other beam conditions, for example, ^{126}Xe at 400 MeV/u and the same power. In the present case, the scaling factor is given by the ratio between the neural network predictions for the initial and final beams conditions, $D(A_f, N_f, E_f)/D(A_i, N_i, E_i)$. The result of this example is shown in Figure 1.6, the scaled dose map (top) and the true calculation for ^{126}Xe (bottom). As can be seen, the scaling method provides a very similar result to the Monte-Carlo calculation that required a computing time of about 24 hours. This means that the linear scaling model is adequate for the present example. The model can be tested further with an extreme case, e.g. ^{208}Pb beam at 50 MeV/u (same power). Figure 1.7 shows the scaled dose-rate map (top) and the true radiation transport calculation (bottom) for ^{208}Pb at 50 MeV/u. As can be seen, the linear scaling factor provides a good result at backward scattering angles (z < -4000 cm). However, the scaled model overestimates the dose-rate at forward angles, in particular at zero degrees. The reason for that is because of the simplicity of the scaling model, which assumes a constant value for all the pixels of the map. In the future, we are planning to extend the model to also account for the angular distributions of the reaction products. For example, we can combine this idea with the use of more robust neural networks such as CNNs (convolutional neural networks) or VAEs (variational autoencoders).

Figure 1.6. Dose-rate map for a ^{126}Xe (400 MeV/u) beam obtained by ML-scaling results from a ^{48}Ca (250 MeV/u) beam, each stopped in copper, with comparison to the dose-rate map calculated by PHITS for the ^{126}Xe beam conditions.

Scaled dose map (top). Dose map calculated with PHITS (bottom)

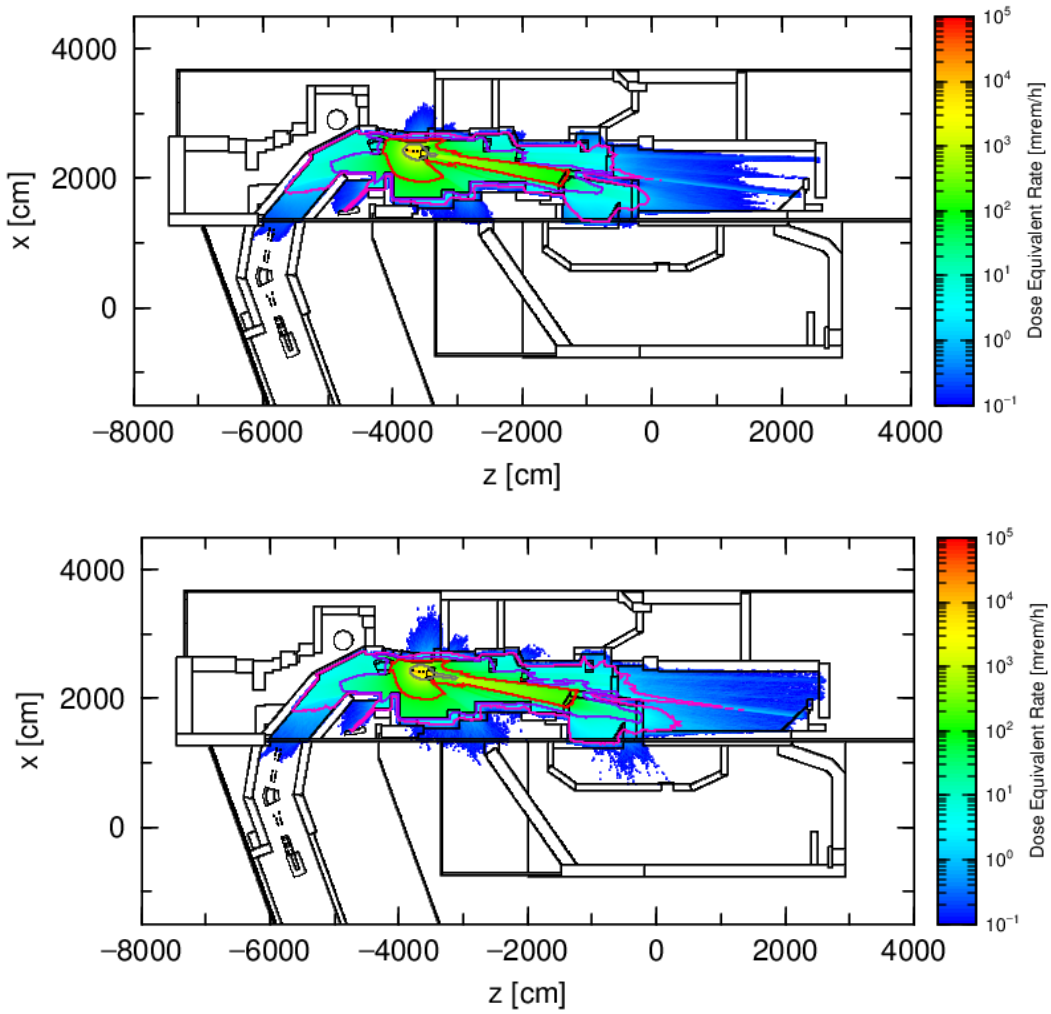

Figure 1.7. Dose-rate map for a ^{208}Pb (50 MeV/u) beam obtained by ML-scaling results from a ^{48}Ca (250 MeV/u) beam, each stopped in copper, with comparison to the dose-rate map calculated by PHITS for the ^{208}Pb beam conditions.

Scaled dose map (top). Dose map calculated with PHITS (bottom)

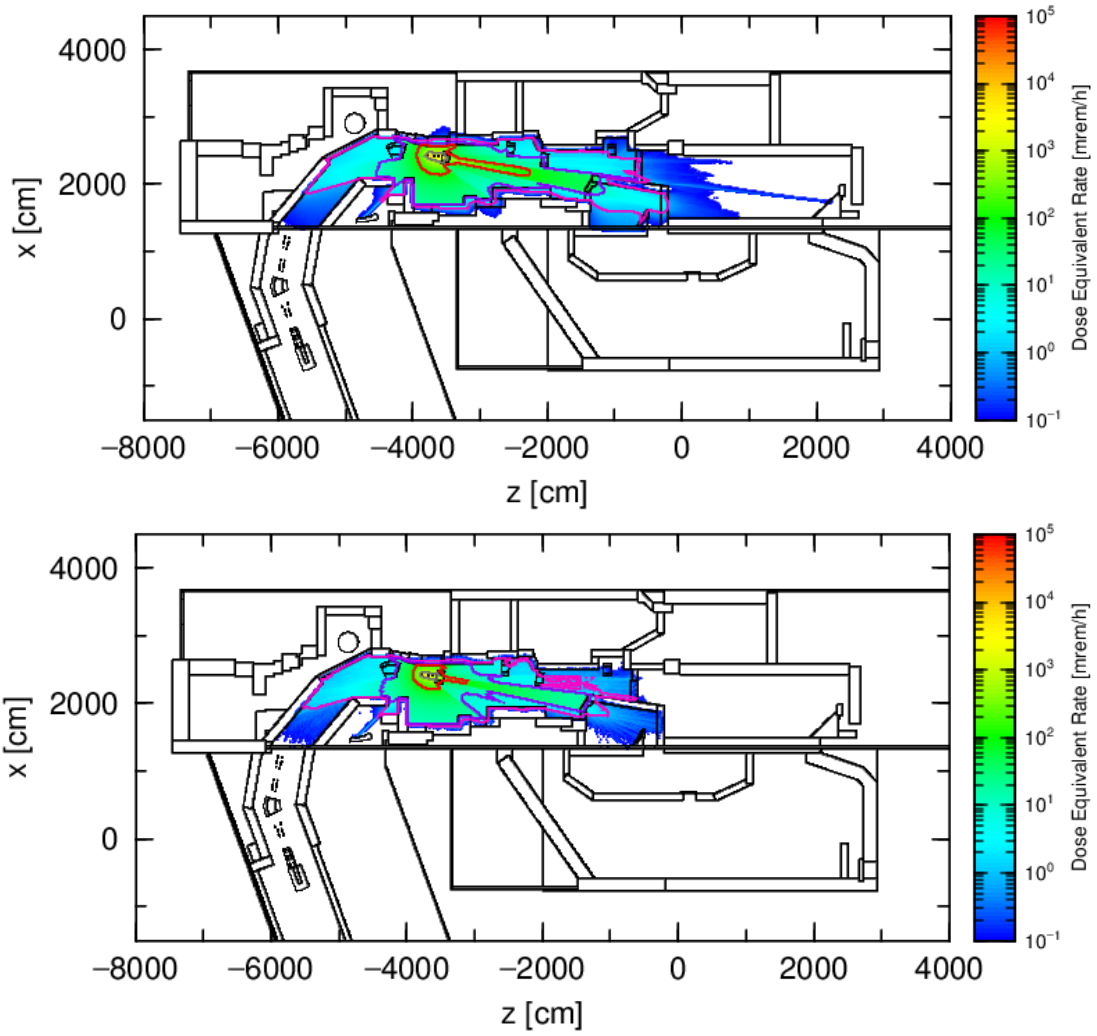

1.5. Summary and Conclusions

A scaling model for radiation transport calculations was developed using machine learning techniques. A large set of PHITS calculations was employed for training neural networks to predict the integrated dose rate at a 1 m distance from the target. The radiation transport calculations for training comprised all the stable isotopes ranging from ^{16}O to ^{208}Pb (238 isotopes) as beam particles at energies from 50 to 400 MeV/u. The model provides a global prediction for any beam particle and initial conditions such as energy and beam power. This allows to normalize dose-rate maps by using linear scaling factors calculated from neural network predictions. The present approximation offers a fast way to generate a dose rate map from an existing radiation transport calculation for any beam isotope and energy. In most of the cases, the scaling model provides satisfactory results compared to time-consuming radiation transport calculations. In the future, a more complete model including

the angular distribution of reaction products will improve the neural network's predictions, which will be particularly important to support radiation transport calculations at FRIB.

1.6. Acknowledgments

This material is based upon work supported by the U.S. Department of Energy, Office of Science, Office of Nuclear Physics and used resources of the Facility for Rare Isotope Beams (FRIB), which is a DOE Office of Science User Facility, operated by Michigan State University, un-der Award Number DE-SC0000661.

1.7. List of references

M. C. Bishop (2006), "Pattern Recognition and Machine Learning (Information Science and Statistics)", Springer-Verlag, Berlin, Heidelberg

D. Castelvecchi (2022), “Long-awaited accelerator ready to explore origins of elements”, Nature 605, 201-203, https://doi.org/10.1038/d41586-022-00711-5

D. P. Kingma and J. Ba (2014), "Adam: A Method for Stochastic Optimization", https://doi.org/10.48550/arXiv.1412.6980

T. Kurosawa et al. (2000), "Neutron yields from thick C, Al, Cu, and Pb targets bombarded by 400 MeV/u Ar, Fe, Xe and 800 MeV/u Si ions", Phys. Rev. C 62, 044615

T. Sato et al. (2018), "Features of Particle and Heavy Ion Transport code System (PHITS) version 3.02", J. Nucl. Sci. Technol. 55, 684-690

1.8. List of abbreviations and acronyms

FRIB	Facility for Rare Isotope Beams
CNN	convolutional neural network
ML	Machine Learning
RT	Radiation transport
VAE	Variational autoencoder

2. Attenuation of Neutrons in Labyrinths: Comparison of Various Calculation Techniques

Dali Georgobiani[1*], Thomas Ginter [2], Nikolai Mokhov [1], Igor Rakhno [1], Michael Vincent [1], Juan Carlos Zamora [2]

[1]Fermi National Accelerator Laboratory, Batavia, IL, USA
[2]Facility for Rare Isotope Beams, Michigan State University, East Lansing, MI, USA
[*]dgeorgob@fnal.gov

To estimate attenuation of accelerator-produced neutrons in labyrinths and penetrations, we use a semi-analytical technique developed at Fermilab, as well as Monte Carlo radiation transport codes MARS, PHITS, and MCNP. The semi-analytical formalism suggests calculating the neutron attenuation factors for the labyrinth legs based merely on the source term at the entrance of the labyrinth; the source term could be either calculated using a Monte Carlo code, or simply estimated from the beam parameters. On the other hand, Monte Carlo codes, with their realistic underlying physics, calculate the radiation environment inside and outside of the labyrinths in great detail. The Monte Carlo results are more reliable, but they are usually computationally expensive. Knowing the relation between the semi-analytical and Monte Carlo results, one can use a more appropriate technique in time-sensitive situations.

2.1. Introduction

Nowadays, estimates of the attenuation of neutron-induced radiation by penetrations involve the use of the powerful Monte-Carlo (MC) radiation transport (RT) codes, where one can build a realistic labyrinth/penetration geometry, use realistic physics for an input and the subsequent analysis, and receive a detailed radiation environment map in and around the labyrinth or penetration as a result of such analysis. Nonetheless, MC calculations, particularly for complex accelerator geometries, can be lengthy and computationally expensive.

Attempts to assess dose rates at the exits of labyrinths or penetrations in accelerator settings historically precede the MC technique-based analysis. Diverse experimental data show that the dose at the labyrinth mouth, or the source term, is in most cases induced by neutrons generated in accelerator and tunnel components. The accelerator beam energy and type have a modest effect on the neutron attenuation in a labyrinth; the only parameter that matters is the total "source" neutron yield that, in turn, depends on the energy and type of the incident particle. Therefore, one can estimate the dose at the exit of a labyrinth using attenuation estimates in each of its legs multiplied by the original dose estimated at its entrance, or mouth. This simple approach makes it straightforward to estimate dose rate at labyrinth or penetration exits. Note that effective dose rates are calculated using both methods; for brevity, we refer to them just as dose rates.

At Fermilab, neutron source term formalism originated in 1976 (see Cossairt, 2016 for a review and a detailed formalism description). In 1991, it was refined to include Moyer model energy scaling. The formalism was implemented in Excel in 1995. Further periodic refinements to the Excel document were made by Vaziri (Vaziri, 2015) and Vincent (Vincent, 2020); these additions include anisotropic source terms, labyrinth leg angular dependence, off-axis sources, and collinear legs.

2.2. Semi-Analytical Model: Labyrinth & Penetration Worksheet

The Labyrinth & Penetration Worksheet, or L&PW (Vincent, 2020), estimates labyrinth or penetration exit dose due to losses in high-energy proton accelerators. Source term inputs include beam energy, number of particles per pulse, and cycle time, as well as loss point geometry with respect to the labyrinth mouth. The source can be calculated within the Worksheet based on generic beam parameters, or estimated empirically, for example harvested from MC calculations. In this work, we use the empirical source calculated using MC codes. Beam power, source term, source-to-mouth distance, Sullivan angle and correction factor, as well as other parameters are calculated automatically within the worksheet. Penetration leg lengths, areas, and angles are specified; then, attenuation for each leg is calculated and applied to the source term, yielding an exit dose at the end of each leg. Attenuation for each leg is first calculated as though that leg was at 90 degrees from the previous leg; if the leg angle differs from 90 degrees, attenuation with the actual angle is then calculated. A schematic view of a labyrinth can be seen in Figure 2.1.

Figure 2.1. Schematic drawing of a three-legged labyrinth (from Cossairt, 2016).

Schematic plan view of a typical three-legged labyrinth at an accelerator facility (from Cossairt, 2016). The star denotes the beam loss location. Geometry parameters used in the semi-analytical approach are shown.

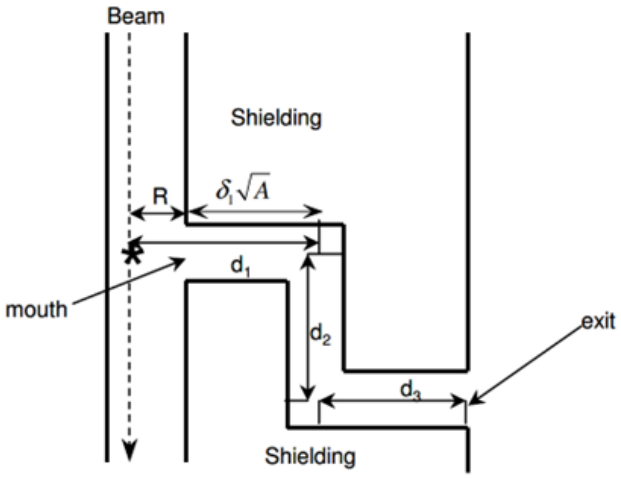

2.3. Simple Radiation Transport Model

A radiation transport model was developed based on a simple geometry (Fig 1.3.1). The model represents a long concrete tunnel, 4 m by 4 m wide, immersed in soil and filled with air; the tunnel concrete walls are 1 m thick. A 4-leg labyrinth filled with air connects the tunnel with the air above the ground surface. The labyrinth is 1 m by 1 m wide, and it is divided into 1 m long air cubes (referred to as AirCubes hereafter) numbered 1 to 15 to simplify the intercomparison between the different calculation methods. AirCube #1 is located inside the tunnel; it is used to collect the initial dose rate that serves as an input for the semi-analytical method. AirCube #15 is located above the ground level.

Figure 2.2. Simple radiation transport model used for Monte-Carlo calculations.

An air-filled labyrinth that connects the tunnel to the air above the ground level is divided into 1m x 1m x 1m cubes (AirCubes) numbered from 1 to 15 for convenience.

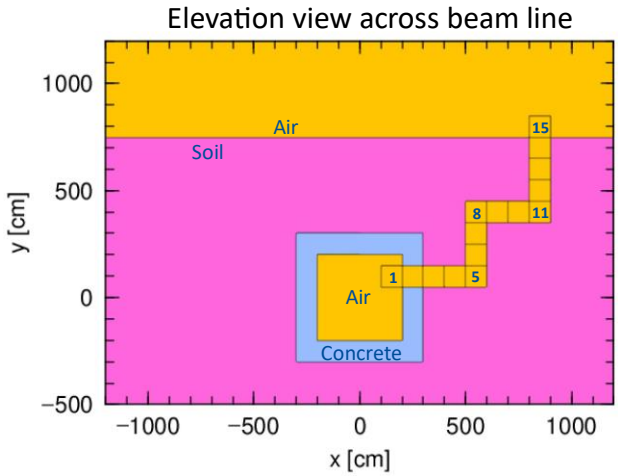

A proton beam at 1 GeV is stopped in a copper cylinder inside the tunnel. The location of the beam stopper (the source) can be right against the labyrinth mouth or at various distances away from it. In this analysis, the source was located 200 cm upstream of the labyrinth mouth. The calculations produce neutron-induced prompt dose rates, neutron fluxes, and energy spectra. Photon-induced prompt dose rates were also calculated, although typically they are significantly lower than neutron-induced ones.

We use 3 major Monte-Carlo codes: MARS15 (Mokhov, 2022), PHITS 3.26 (Sato et al, 2018), and MCNPX 2.6 (Pelowitz, 2014). We implement variance reduction techniques to speed up our calculations: importance splitting in a form of branching in MARS, weight windows in PHITS, and dxtran spheres in MCNPX. All Monte-Carlo calculations were produced within a "reasonable" time frame – 2-3 days wall time at most (for example, 3 days at a Linux cluster with 64 nodes for MARS calculations).

2.4. Calculation Results and Analysis

2.4.1. Prompt dose rate maps

Neutron- and photon-induced dose rate maps across the tunnel, at the location of the labyrinth, are shown in Figure 2.3 for MARS calculations, Figure 2.4 for PHITS calculations, and Figure 2.5 for MCNP calculations. One can see that neutron-induced doses are significantly higher than photon-induced ones.

Figure 2.3. Prompt dose rate maps calculated by MARS.

Left panel: Neutron-induced dose rates; Right panel: Photon-induced dose rates.

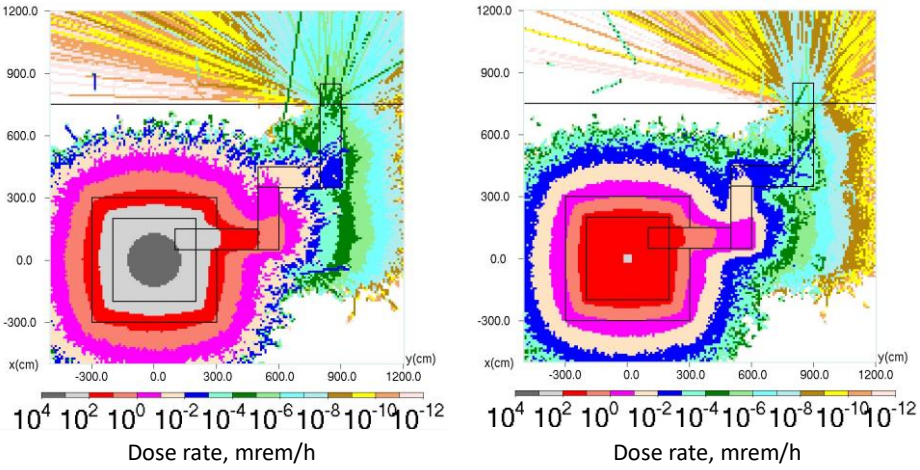

Figure 2.4. Prompt dose rate maps calculated by PHITS.

Left panel: Neutron-induced dose rates; Right panel: Photon-induced dose rates.

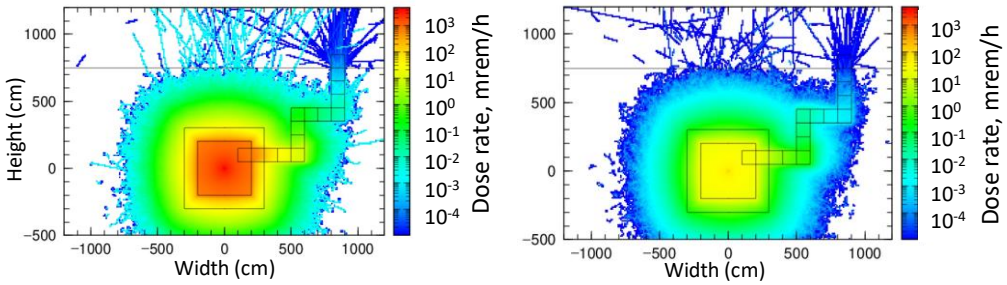

Figure 2.5. Prompt dose rate maps calculated by MCNP.

Left panel: Neutron-induced dose rates; Right panel: Photon-induced dose rates. Note that the maximum dose rate in the right panel is ~100 times lower than the maximum dose rate in the left panel.

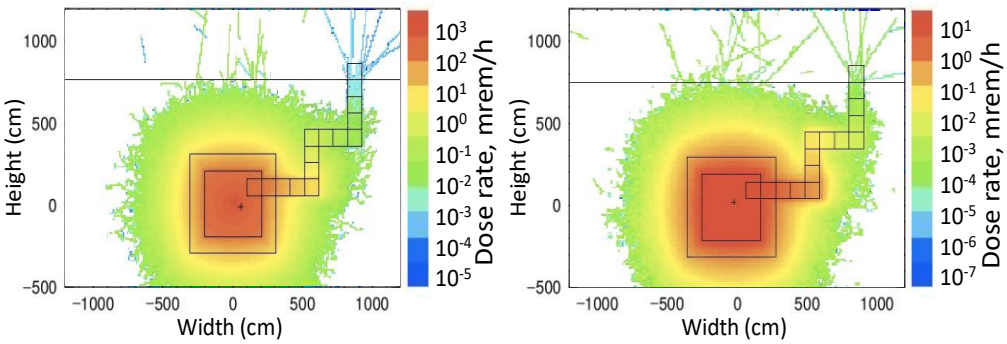

2.4.2. Comparison between MC and L&PW results

Taking the MC-calculated dose rate in the AirCube #1 as the source term, we use the Labyrinth & Penetration Worksheet to calculate prompt dose rates at labyrinth turns (AirCubes #5, #8, #11) and the AirCube #15 that is located above the ground level (see Figure 1.3.1). We calculate dose rates in each cube using the Monte-Carlo codes. Figure 2.6 shows the comparison of these results, while Figure 2.7 shows the ratios of the MC results. Comparison among the MC results shows that: MARS and PHITS results are very close in the first legs (good statistics, relative errors are below few percent); MCNP produces slightly lower doses. In successive legs, statistics go down (errors could be as high as 50%), and the results from the different codes somewhat diverge. Comparison of the MC results to the L&PW outcome demonstrates that L&PW results are up to 10 times higher in the first and second labyrinth bends, but they become very close to each other in the successive bends.

We conclude that, in the first and second labyrinth legs, L&PW results are **conservative** compared to MC results. In successive legs, L&PW results are **similar** to MC results.

Figure 2.6. Neutron-induced dose rates: Comparison of the MC code results to the LPW results in AirCubes.

Error bars for the MC code results have the same colours as the MC result lines.

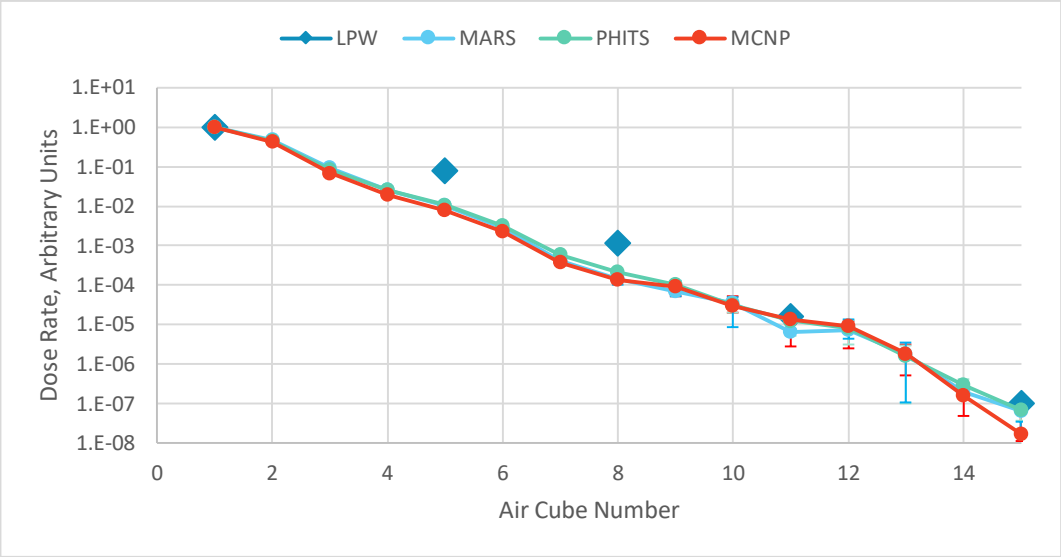

Figure 2.7 Neutron-induced dose rates: Ratio of the MC code results to the LPW results in AirCubes.

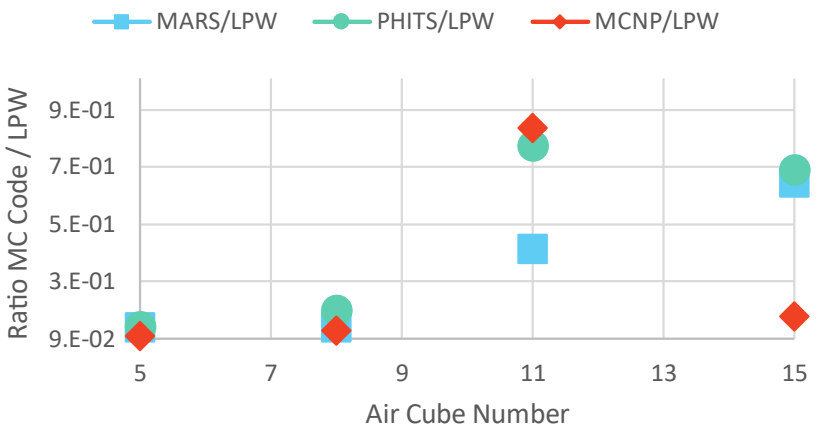

2.4.3. Neutron- and photon-induced dose rates from MC code applications

Figures 2.8, 2.9, and 2.10 show prompt dose rates in the AirCubes separated into neutron and photon contributions and calculated by means of the Monte-Carlo codes. The neutron-induced dose rates are at least an order of magnitude higher than photon-induced dose rates; this difference goes down as neutrons lose energy in the successive labyrinth legs. MARS allows the calculation of the so-called total dose – it includes contributions from other particles besides neutrons (protons, photons, electrons, pions, kaons, muons). Proton contributions dominate close to the radiation source. At regions of the labyrinth farther removed from the source, there is a noticeable enhancement of the photon-induced dose in comparison with the neutron-induced dose. This effect could result from the decrease of neutron energy along the labyrinth path leading to an increase in neutron capture which in turn leads to an increase in photon flux (see Figure 2.10 where this effect is the most pronounced).

Figure 2.8. MARS results: Comparison of neutron- and photon-induced dose rates. Total dose rate is dominated by the proton contribution close to the source.

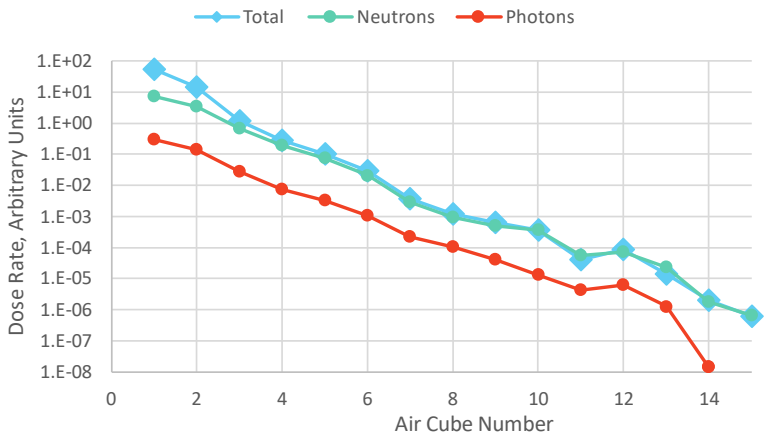

Figure 2.9. PHITS results: Comparison of neutron- and photon-induced dose rates.

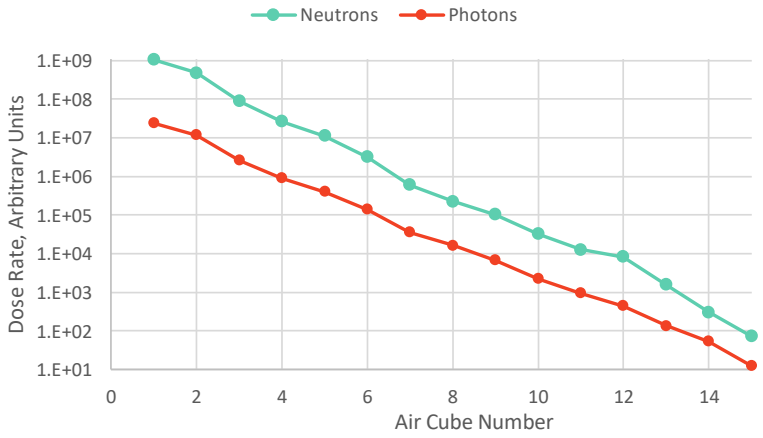

Figure 2.10. MCNPX results: Comparison of neutron- and photon-induced dose rates.

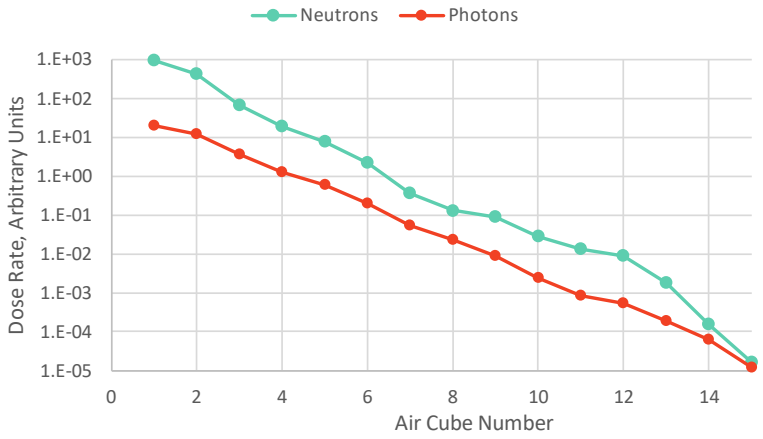

2.4.4. Neutron fluxes and energy spectra

We estimate neutron fluxes (Figure 2.11) and energy spectra (Figure 2.12) using MC codes. The PHITS results are presented here; other codes give very similar outcomes. One can see that neutron energy spectra become softer after the first labyrinth leg; neutrons reaching the ground surface are completely thermalized. Attenuation factors are larger than an order of magnitude in each successive leg, with the total attenuation factor reaching 5E5.

Figure 2.11. PHITS results: Neutron fluxes in the AirCubes.

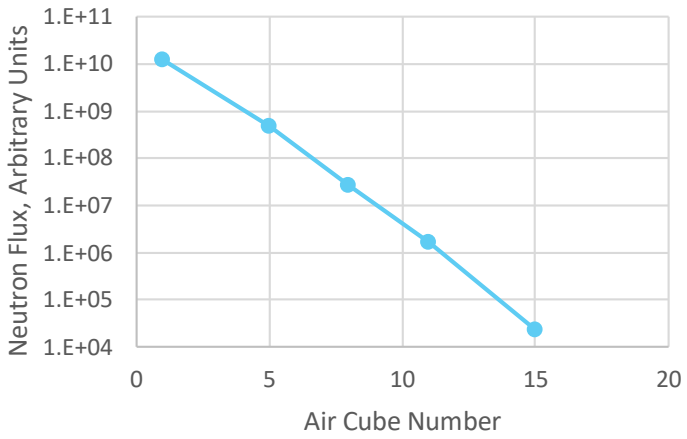

Figure 2.12. PHITS results: Neutron energy spectra in the AirCubes.

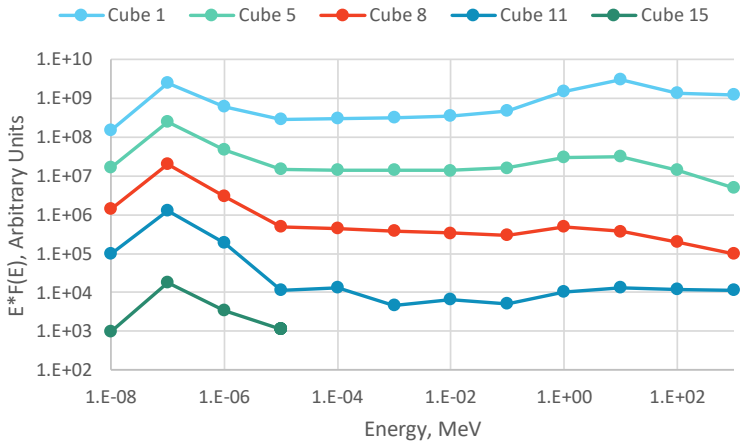

2.4.5. MARS dose rate calculations using realistic facility models

Monte-Carlo codes are commonly used to estimate radiation environments at various facilities. Monte-Carlo calculations using large, sophisticated facility models with realistic geometry and details demand significant computing power and time commitment; they utilize multiprocessor jobs that take days or weeks. Figure 2.13 shows examples of the prompt dose rate distributions in the Fermilab PIP-II Project tunnel areas, under an accident scenario condition, calculated using a realistic PIP-II model (Pozdeyev et al., 2022). One can see that the labyrinths (RF penetrations) on the right-hand side of the main tunnel are not well-populated even after long calculations.

Figure 2.13. MARS results: Prompt dose rates in the Fermilab PIP-II tunnel areas.

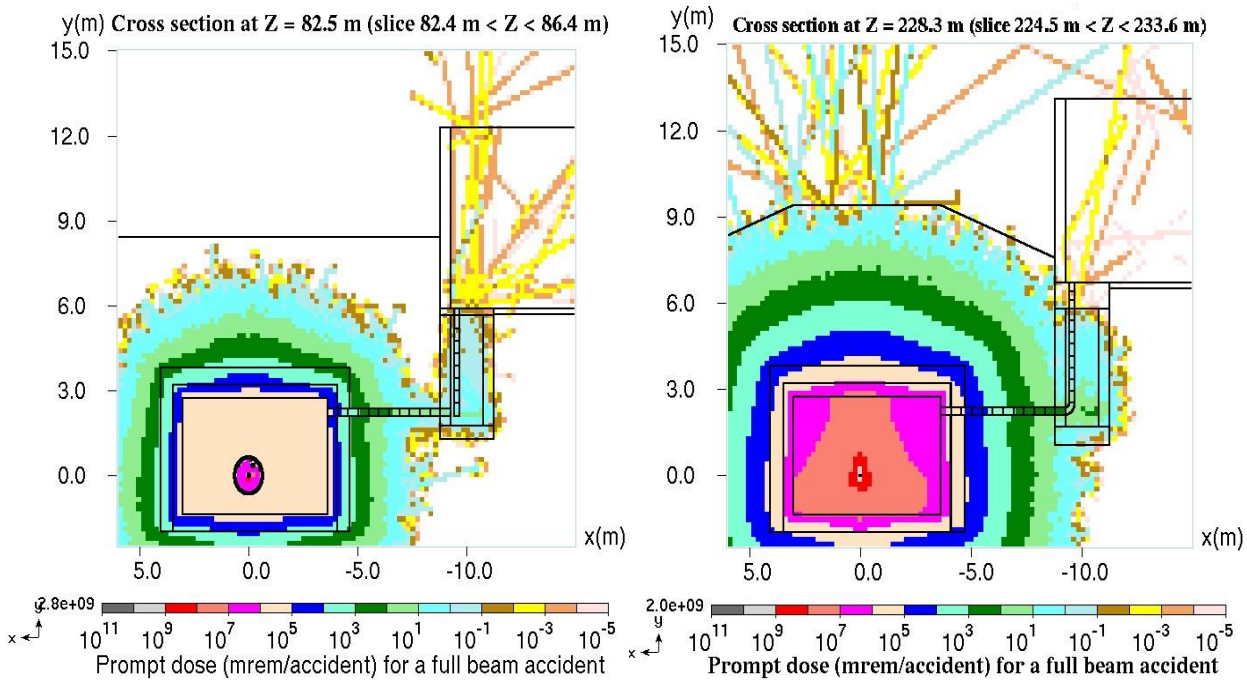

2.5. Discussion

There are several observations that one could make based on the comparison results.

In the current analysis, the source was placed 2 m away from the labyrinth mouth; a quick calculation with the source placed against the labyrinth mouth brought the L&PW and MC results much closer together, with a ratio between them of about 4 at most.

There is a discussion on whether the empirical source should be collected at the AirCube #1 (in front of the labyrinth mouth) or the AirCube #2 (inside the labyrinth mouth). Analysing the second possibility, we observe that the discrepancy between the MC and L&PW results in the first two labyrinth legs reduced to about factor of 5.

Neutron-induced dose is higher than photon-induced dose by at least a factor of 10 or more at the labyrinth mouth. Photon-induced dose rates produce a closer match between the MC and L&PW results. Ratios between neutron-induced and photon-induced doses reduce with successive legs as neutrons lose energy in multiple scatterings; on the other hand, the total dose keeps falling, so overall photon contribution is not significant even far from the source.

The results from all three MC codes match well throughout most of the labyrinth. The discrepancy begins farther from the source – after the second leg – and could be partially attributed to insufficient statistics.

Other particles (mostly protons) contribute to the total dose rates within the tunnel, but their contribution falls off very fast inside the labyrinth.

2.6. Path Forward

In this work, we considered a single scenario out of many possible scenarios. Various other possibilities could be considered: one could vary the input parameters, such as the proton energy and the source location with respect to the labyrinth mouth. The L&PW calculations can be performed using the beam input parameters instead of the MC code-produced dose rates at the labyrinth mouth (a quick estimate shows that the results of this approach are very close to the results shown here). Also, the labyrinth parameters can be changed in the simple model to match a more realistic labyrinth geometry: for example, to make the labyrinth 1 m by 2 m wide, or a typical door size, just as outlined in Cossairt's formalism. Flux-to-dose (FTD) conversion coefficients could be another source of discrepancy since every code uses a different set of FTD coefficients. One could choose a particular FTD set and use it in all Monte-Carlo calculations to rule out this factor.

2.7. Summary and Conclusions

We study the attenuation of accelerator-produced neutrons in labyrinths and penetrations using both the semi-analytical method developed at Fermilab, and the Monte-Carlo radiation transport codes MARS, PHITS, and MCNP. We build a simple labyrinth model and analyse it using both approaches. A 1 GeV proton beam on a copper target was used to produce a radiation field in the tunnel and the labyrinth; a realistic beam type and energy, as well as a realistic tunnel/labyrinth geometry and materials were chosen to be comparable to common Fermilab parameters. Neutron- and photon-induced dose rates were estimated in the labyrinth using both the semi-analytical and Monte-Carlo methods. Neutron and photon fluxes and energy spectra were also estimated using MC methods.

Results of the semi-analytical method are conservative in comparison to the Monte-Carlo results for the first and second labyrinth legs. For successive legs, the two results are very similar. Neutrons become completely thermalized after the third leg. Photon contributions to the total dose are at least an order of magnitude lower than neutron contributions.

2.8. List of references

E. Pozdeyev et al. (2022), "PIP-II Linac Complex Preliminary Shielding Assessment", FNAL

J. D. Cossairt (2013), "Approximate Technique for Estimating Labyrinth Attenuation of Accelerator-Produced Neutrons", Fermilab Radiation Physics Note 118, Revision 1

J. D. Cossairt (2016), "Radiation Physics for Personnel and Environmental Protection", Fermilab Report TM-1834, Revision 15

N. V. Mokhov and C. C. James (2017), "The MARS Code System User's Guide", Version 15, Fermilab-FN-1058-APC; https://mars.fnal.gov

N. V. Mokhov (2022), "MARS15 Code Overview"

D. B. Pelowitz, A. J. Fallgren, G. E. McMath (editors) (2014), "MCNP6 User's Manual, Code version 6.1.1beta", Los Alamos National Laboratory, LA-CP-14-00745, Rev. 0.

T. Sato et al. (2018), "Features of Particle and Heavy Ion Transport code System (PHITS) version 3.02", J. Nucl. Sci. Technol. 55, 684-690

K. Vaziri (2015), "Dose Attenuation Approximation along a Labyrinth, Penetrations and Tunnels", Fermilab Radiation Physics Note 140, Revision 2

M. Vincent (2020), “Modifications to the Labyrinth & Penetration Worksheet”, FNAL Draft Document

2.9. Acknowledgements

DG would like to express her gratitude to the SATIF-15 LOC and SOC members, the Session Chairs, the FRIB Management and Administrative Personnel for their support and assistance in organizing the Workshop.

This work is supported by Fermi Research Alliance, LLC under contract No. DE-AC02-07CH11359 with the U.S. Department of Energy. This research used, in part, ALCC allocations at the Argonne Leadership Computing Facility (ALCF) and at the National Energy Research Scientific Computing Center (NERSC) which are DOE Office of Science User Facilities supported under Contracts DE-AC02-06CH11357 and DE-AC02-05CH11231, respectively.

2.10. List of abbreviations and acronyms

L&PW	Labyrinth & Penetration Worksheet
MC (RT) code	Monte-Carlo (Radiation Transport) code
PIP-II	Proton Improvement Plan II – a project at Fermilab, USA

3. Inter-comparison of particle production (4)

Hideo Hirayama[1,2]* and Toshiya Sanami[1]
[1]KEK, High Energy Accelerator Research Organization
[2]Nuclear Regulation Authority
*hideo.hirayama@kek.jp

We propose new inter-comparison problems of particle production from targets to find the reason for the relatively large differences between codes in neutron production as presented at SATIF-14.

In addition to neutrons, protons, charged positive pions, charged negative pions and photons above 20 MeV from 10 GeV protons are requested to calculate in the revised problem.

At SATIF-15, we will present a comparison between the major Monte Carlo codes sent from contributors for this inter-comparison.

3.1. Introduction

At SATIF-14, we showed the following results between PHITS, Geant4, MCNPX, MARS and FLUKA:

(a) The differences between codes are less than a factor 2 for total neutrons and total neutron energies above 20 MeV emitted from the target.

(b) Relatively large differences exist in the comparison of the angular spectra especially at 0 degrees.

For SATIF-15, the revised problems were sent to all contributors to understand the reasons for the large differences.

3.2. Problems for an Inter-comparison at SATIF-15

1.2.1. Incident particle

Pencil beam of protons with 10 GeV.

1.2.2. Target materials and their sizes

Target geometry is the cylinder.

Source protons incident on the center of the cylinder bottom.

Target detector distance from the center of the cylinder is 500cm.

(a) Al : length 40cm, diameter 4.0cm and density 2.7g/cm^3

(b) Cu : length 16cm, diameter 1.6cm and density 8.63 g/cm^3

(c) Au : length 10cm, diameter 1.0cm and density 19.3 g/cm^3

1.2.3. Quantities to be calculated

(1) Neutron, proton, charged positive pion, charged negative pion and photon spectra above 20 MeV in particles/ MeV/sr/proton

at 0, 15, 30, 45, 60, 90, 120, 150 degrees with an angular width of ±0.5 degrees.

Photons from produced radionuclides are not necessary to include.

(2) Angular integral spectrum in particles/ MeV/proton

(3) Energy integral fluences for (1) and (2) in particles/proton

1.2.4. Calculated results must be sent to H. Hirayama at KEK (hideo.hirayama@kek.jp) with the following data till June 30 of 2022 to prepare the inter-comparison.

(a) Name of participants and organization

(b) Name of the computer code used for calculations

(c) Name of data base used in the code

3.3. Summary of Contributors

Table 3.1. lists the participants, the names of the computer codes and the database, and the physical model used. In the case of Geant4, the results with four models were almost the same. Therefore, the results using the "Shielding" model only were used for the comparison.

3.4. Results and Discussions

3.4.1. Comparison of particle fluence above 20 MeV

A comparison between the codes is presented in the form of tables to clearly show the differences. Table 3.2. shows the total particle fluence above 20 MeV and Table 3.3., 3.4., 3.5., 3.6. and 3.7. show the angular fluence above 20 MeV for neutrons, protons, charged positive pions, charged negative pions and photon, respectively. The ratio of the maximum value (in red) to the minimum value (in blue) in each case is also shown in the table. The ratios of the maximum and minimum values for the angular fluence are also shown in Figures 3.1., 3.2., and 3.3. for Al, Cu and Au, respectively.

From these tables and figures following tendencies can be obtained.

(1) The differences in total particle fluence number above 20 MeV are similar between neutrons, protons, charged positive pions, charged negative pions and photons for Al, Cu and Au. Max/min values are scattered from 1.28 (proton from Al target) to 1.80 (neutron from Au target).

(2) Large differences exist in the energy integral angular fluence especially at 0 degrees and above 90 degrees for neutrons and protons. The max/min values almost exceed 2 at large angles.

(3) The differences in integral angular fluence in charged positive pions, charged negative pions and photons are smaller than those in neutrons and protons. The same tendencies with neutrons and protons to increase the differences at 0 degrees and above 90 degrees are observed in these particles with smaller max/min values.

3.4.2. Comparison of particle spectrum above 20 MeV

Figures 3.4. and 3.5. show the neutron spectra above 20 MeV at 0 degrees and 150 degrees, respectively. Figures 3.6. and 3.7. show the proton spectra above 20 MeV at 0 degrees and 150 degrees, respectively. Figures 3.8. and 3.9. show the charged positive pion spectra

above 20 MeV at 0 degree and 150 degrees, respectively. Figures 3.10. and 3.11. show the charged negative pion spectra above 20 MeV at 0 degrees and 150 degrees, respectively. Figures 3.12. and 3.13. show the photon spectra above 20 MeV at 0 degrees and 150 degrees, respectively. The differences in spectra shape of charged positive pions, charged negative pions and photons are smaller than those of neutrons and protons. Figure 3.14. shows the neutron spectrum from the Al target, proton spectrum from the Cu target, and charged positive pion spectrum from the Au target at 30 degrees as an example of comparison at another angle, respectively. As shown in this figure, the differences in the spectra are smaller at 15, 30, and 60 degrees in comparison with those at 0 degrees and above 90 degrees.

3.5. Summary and Conclusions

From the comparisons shown the above, we can summarize the following results:

(1) The differences in the energy integral angular distribution above 20 MeV between code are remarkable at 0 degrees and above 90 degrees for neutrons and protons from the Al, Cu and Au targets.

(2) The differences in the energy integral angular distribution above 20 MeV between code for charged positive pion, charged negative pion and photon are smaller than those for neutrons and protons, but show a similar tendency to increase at 0 degree and above 90 degrees.

(3) Similar tendencies were observed for the differences in the particle spectra. The differences in the spectrum are smaller at 15, 30 and 60 degrees.

The Following actions are proposed for the next meeting:

(1) The developers of each code should check the model considering the results of this inter-comparison and send revised results to the organizer until the next meeting.

(2) It is desirable to include the results of MCNP6 and MARS.

3.6. List of references

H. Hirayama and T. Sanami, “Intercomparison of particle production”, Proceedings of 14th Specialists’ workshop on Shielding aspects of Accelerators and Targets, and Irradiation Facilities (SATIF-14), Gyeongju, Korea, October 30 - November 2, 2018, OECD NEA/NSC/R(2021)2, pp.222-278.

Figure 3.1. Max/Min of energy integrated (> 20 MeV) angular fluence, Al

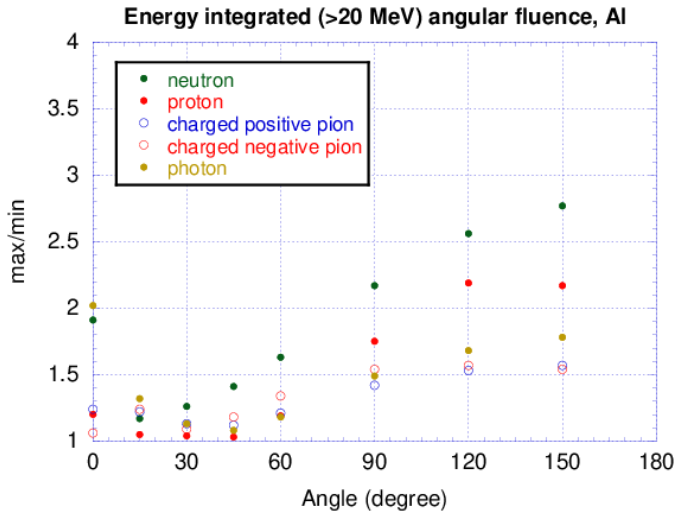

Figure 3.2. Max/Min of energy integrated (> 20 MeV) angular fluence, Cu

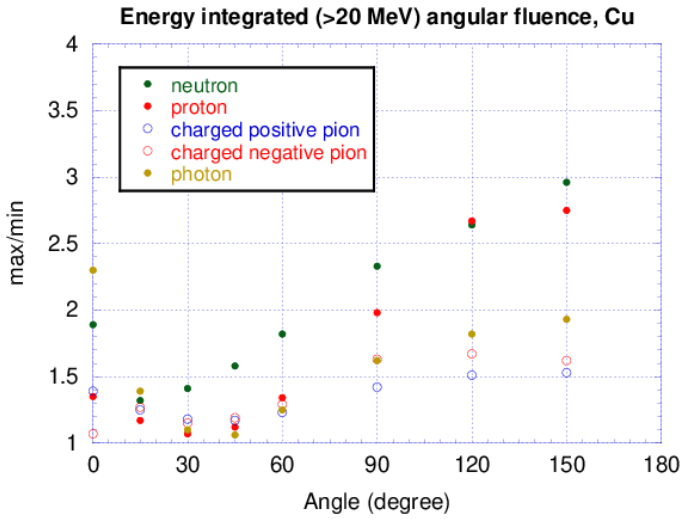

Figure 1.3. Max/Min of energy integrated (> 20 MeV) angular fluence, Au

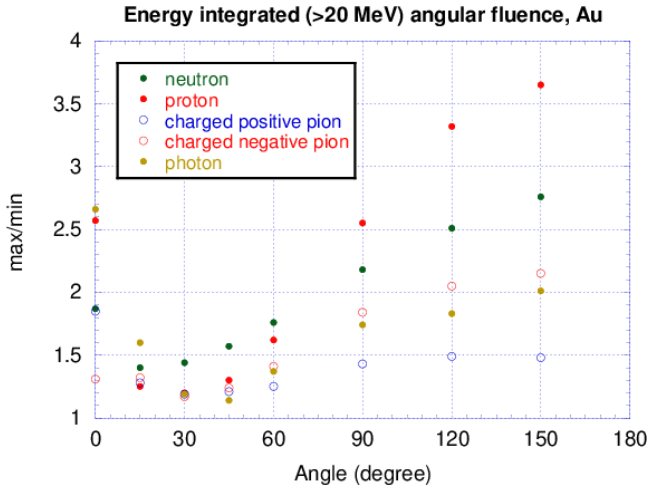

Figure 3.4. Comparison of neutron spectra at 0 degrees

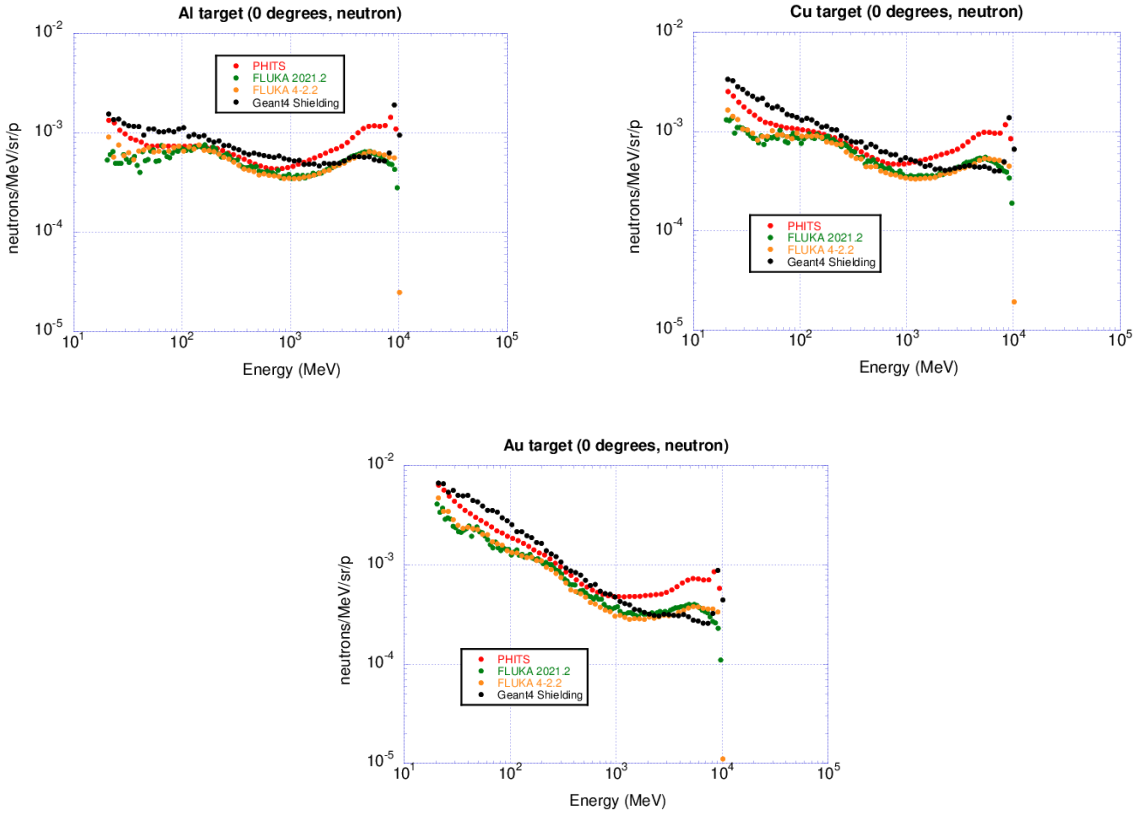

Figure 3.5. Comparison of neutron spectra at 150 degrees

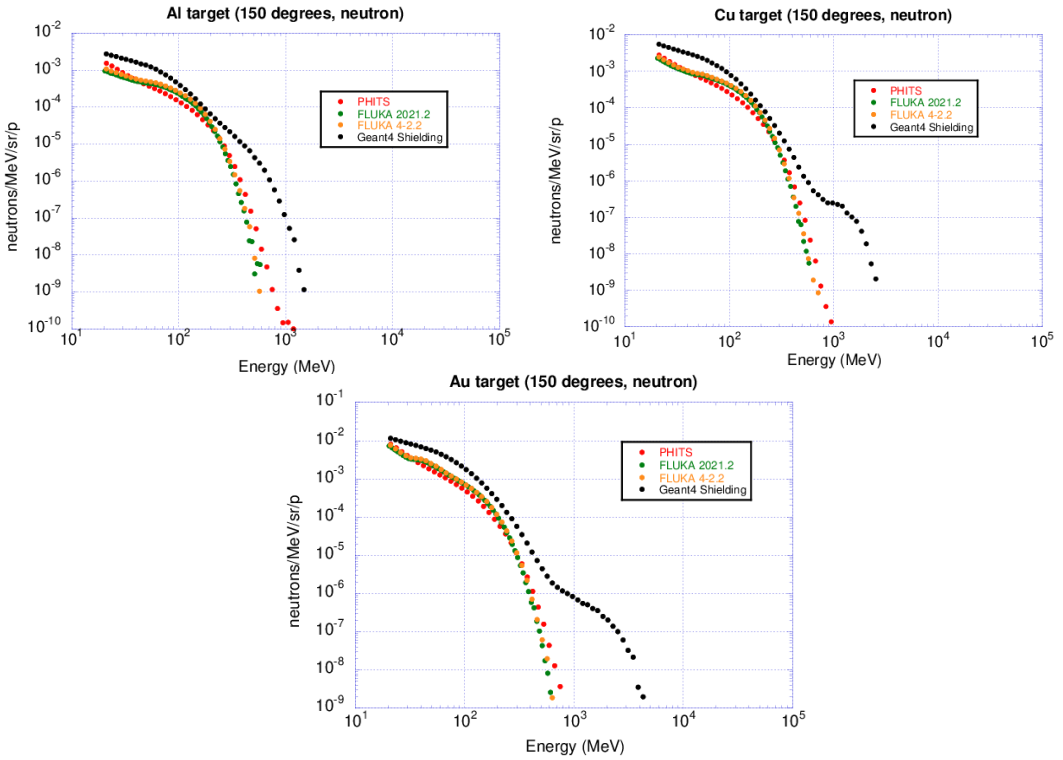

Figure 3.6. Comparison of proton spectra at 0 degrees

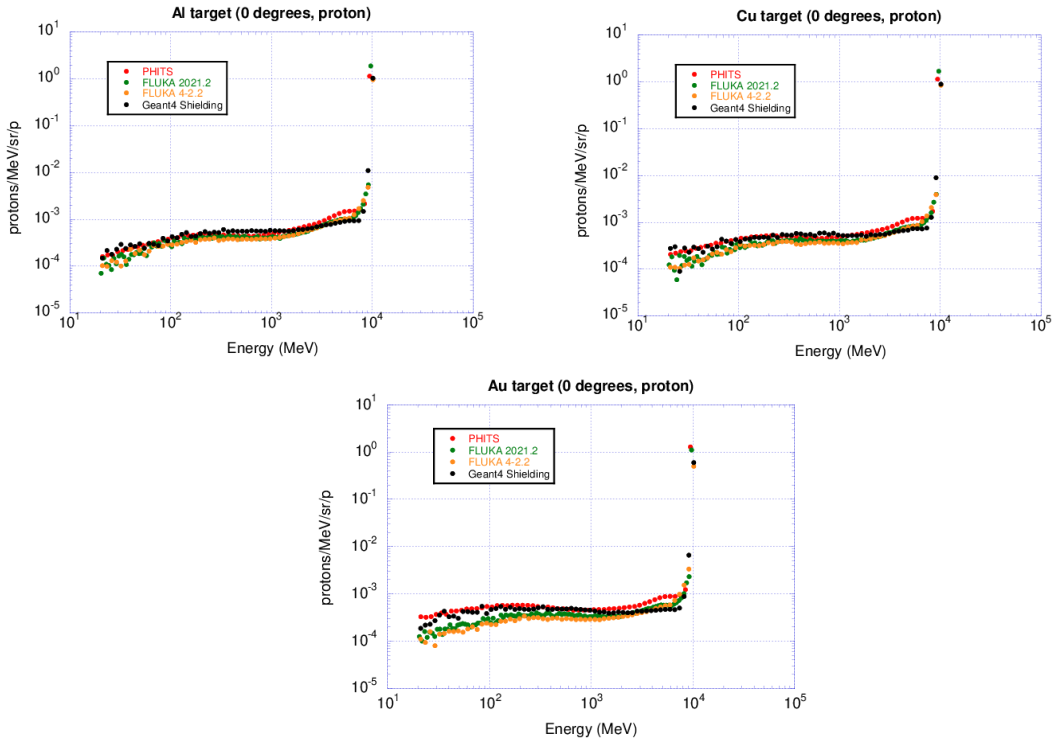

Figure 3.7. Comparison of proton spectra at 150 degrees

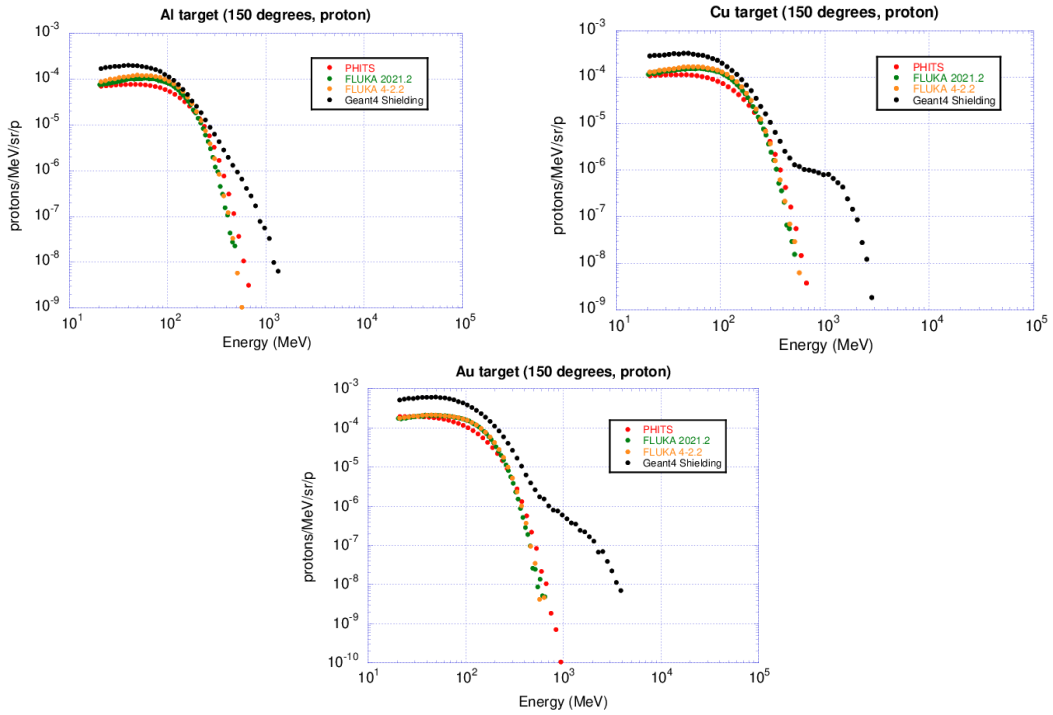

Figure 3.8. Comparison of charged positive pion spectra at 0 degrees

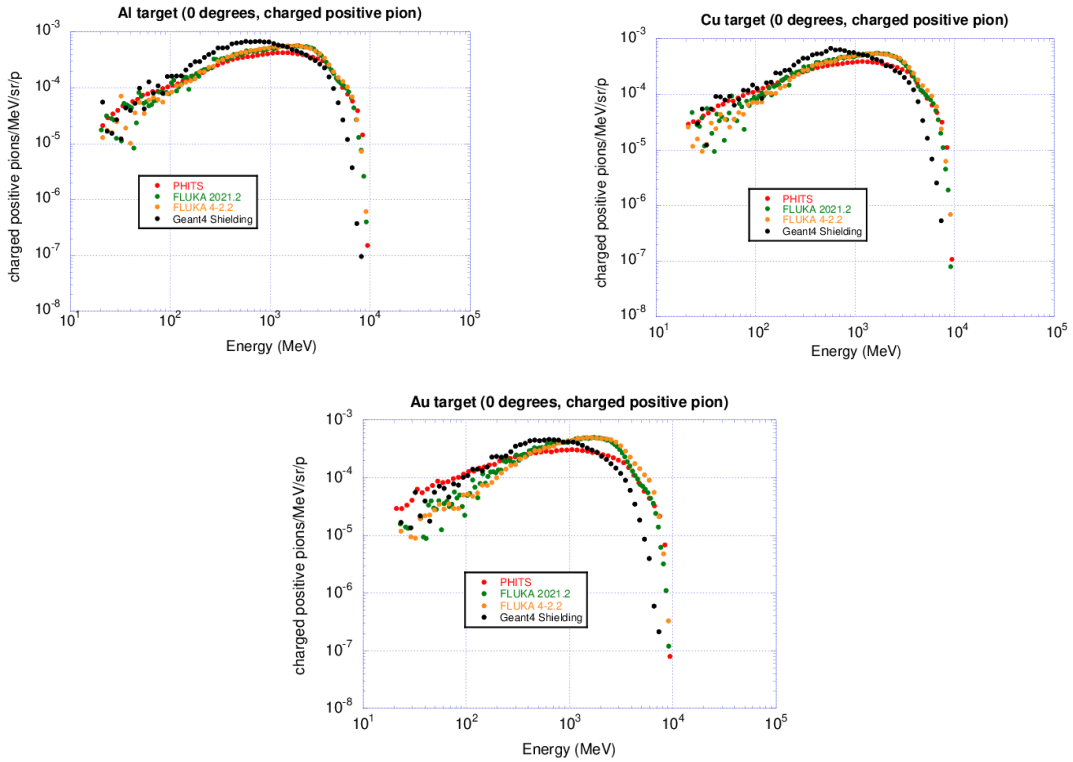

Figure 3.9. Comparison of charged positive pion spectra at 150 degrees

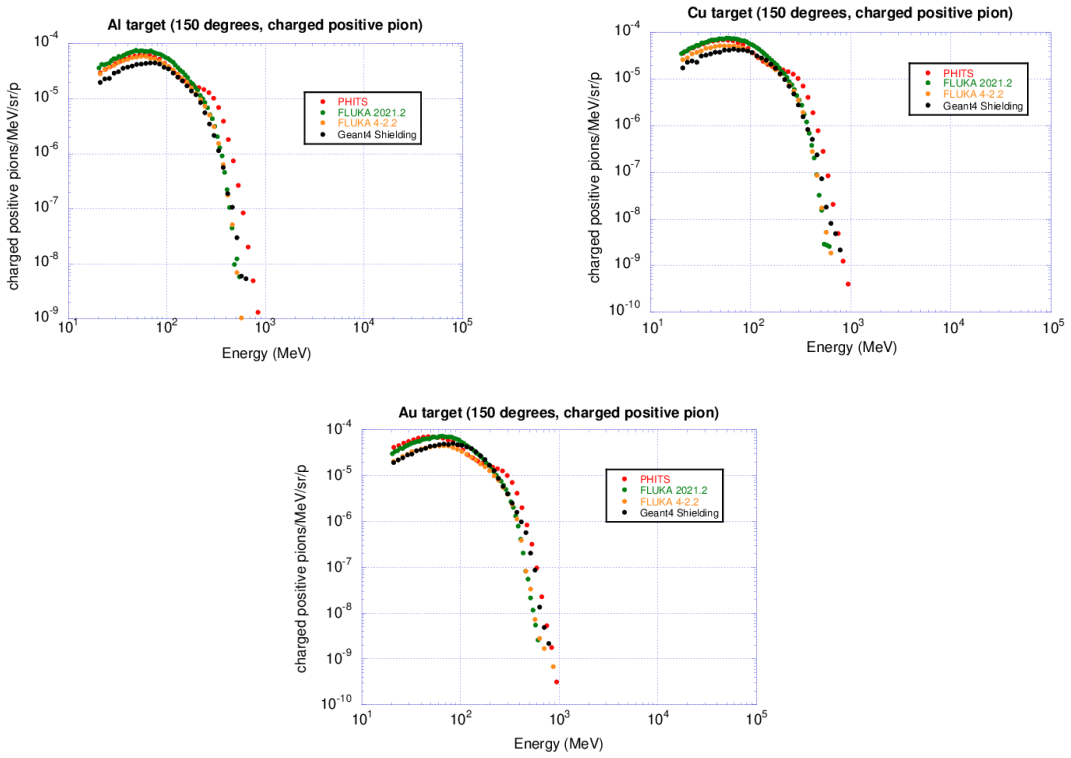

Figure 3.20. Comparison of charged negative pion spectra at 0 degrees

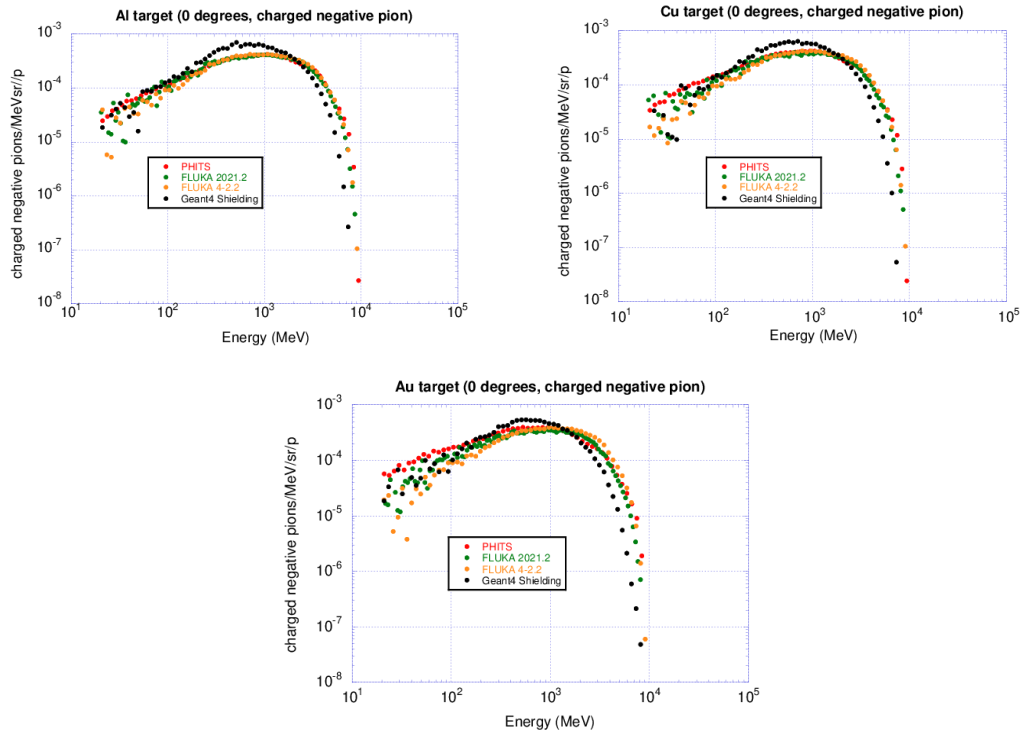

Figure 3.31. Comparison of charged negative pion spectra at 150 degrees

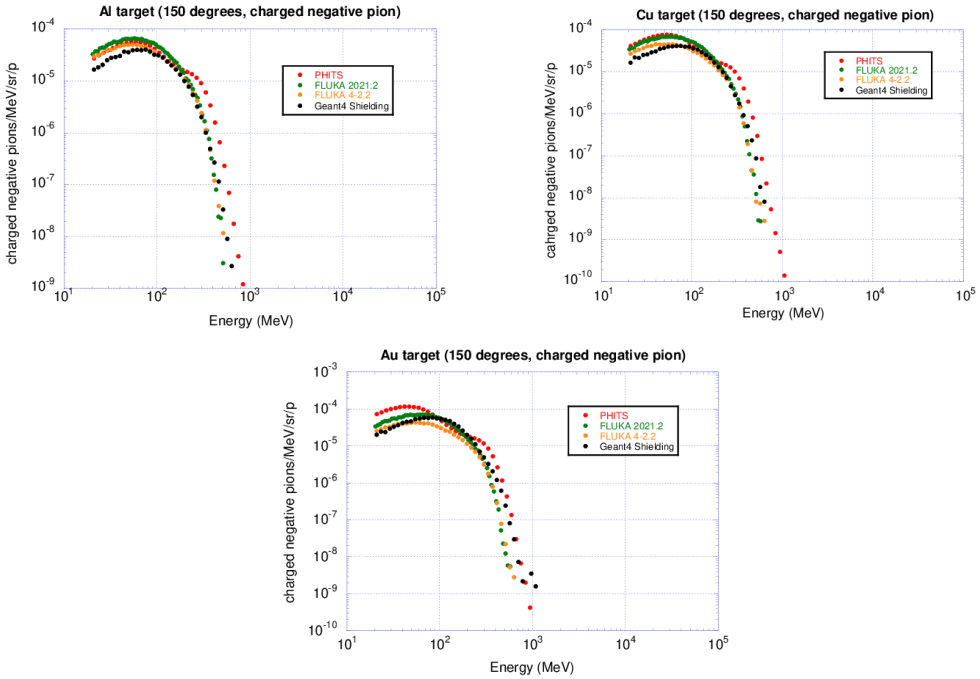

Figure 3.42. Comparison of photon spectra at 0 degrees

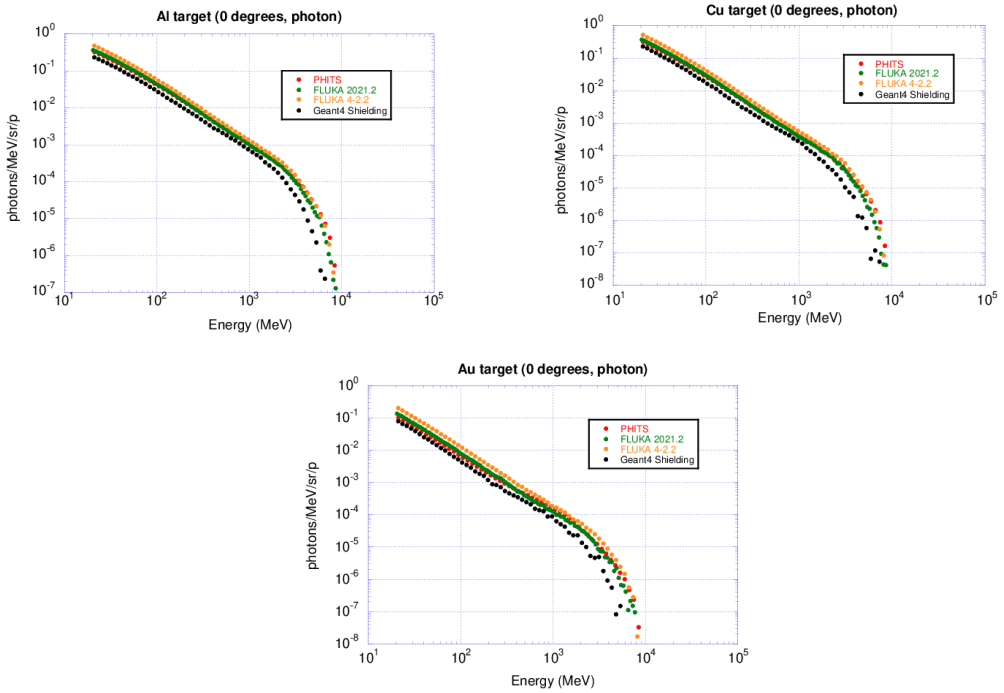

Figure 3.13. Comparison of photon spectra at 150 degrees

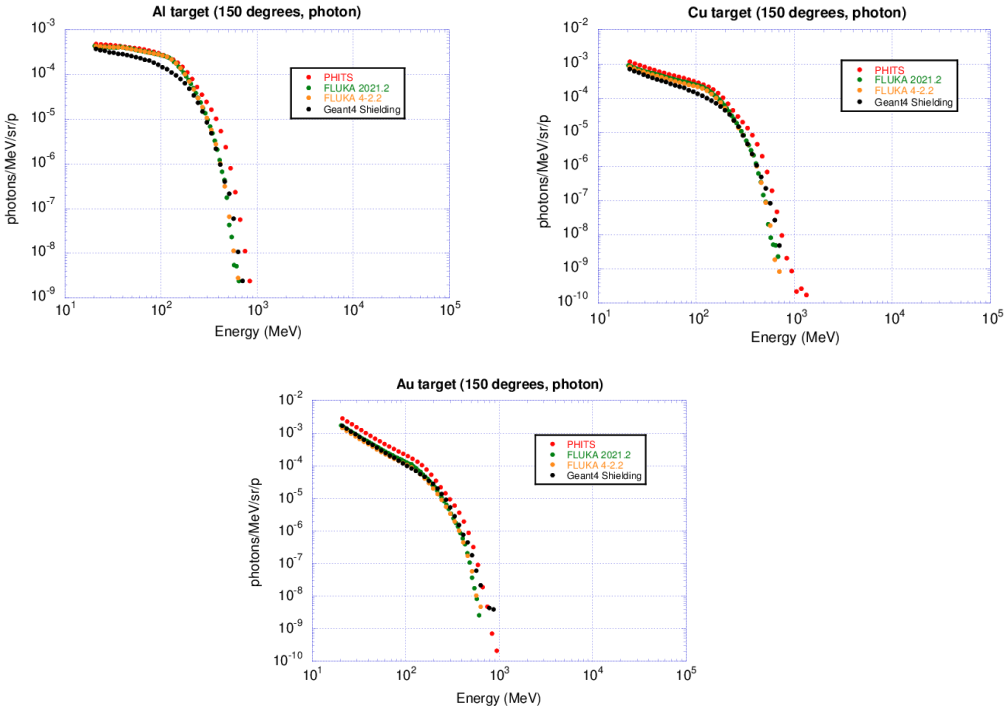

Figure 3.14. Comparison of spectra at 30 degrees

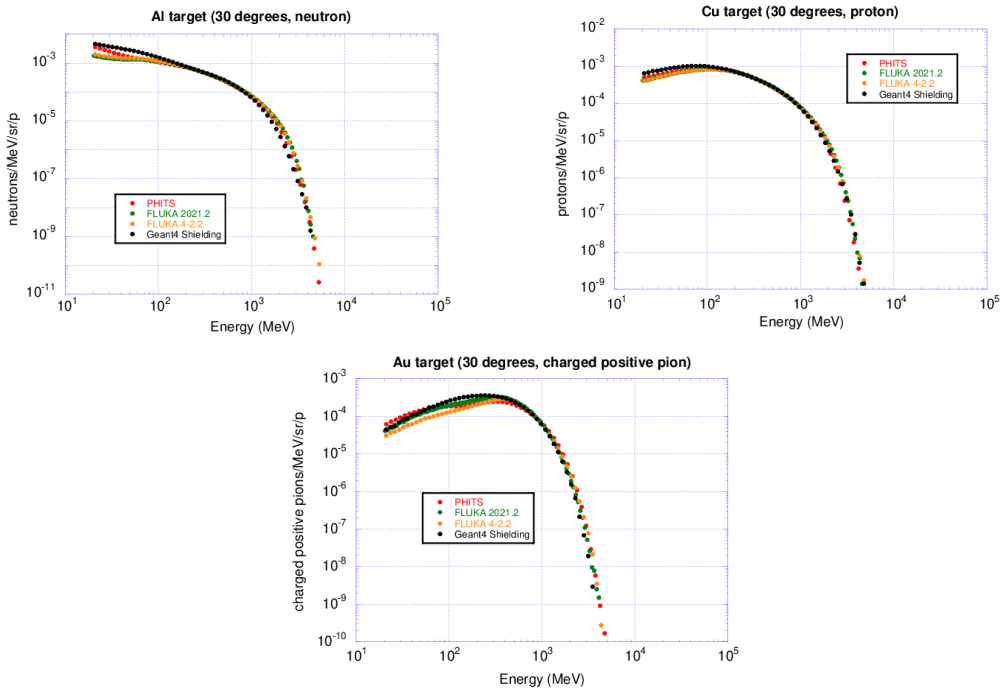

Table 3.1. Summary of contributors for particle production calculation (4)

Name of participants and organizations	Code	Data Base	Physical model
N. Matsuda (JAEA) and PHITS group	PHITS	Original (PHITS)	INCL4.6(<3GeV)+JAM(>3GeV)
A.Fasso`, .Ferrari, .Ranft*, P.R.Sala (*deceased) The FLUKA Collaboration	FLUKA Version 2021.2	None for charged particles and neutrons above 20 MeV (models only)	
R. Froeschl, V. ouskoura, S. Roesler (CERN)	FLUKA Version 4-2.2		
A. D. Servelle(1,2), G. Hugo(1), V. Iachoudis(1), A. Ribon(1) (1) CERN, (2) EPFL)	Geant4 version 11.0.2		(1) FTFP_BERT_HP (2) QGSP_BERT_HP (3) QGSP_BIC_HP (4) Shielding

Table 3.2. Comparison of total particle fluence number above 20 MeV

	Name of code	Geant4 Shielding	PHITS	FLUKA 2021.2	FLUKA 4-2.2	
	Particle	Particles (>20 MeV) /proton				max/min
Al	neutron	2.36	2.35	2.12	1.53	1.54
	proton	1.51	1.93	1.90	1.33	1.28
	charged positive pion	0.591	0.852	0.955	0.598	1.62
	charged negative pion	0.505	0.750	0.805	0.496	1.59
	photon	2.22	3.50	3.66	2.85	1.65
Cu	neutron	2.11	3.29	2.94	2.69	1.56
	proton	1.85	2.16	2.11	1.46	1.48
	charged positive pion	0.586	0.839	0.941	1.22	1.67
	charged negative pion	0.530	0.807	0.829	0.496	1.67
	photon	2.90	4.54	4.65	3.71	1.60
Au	neutron	6.73	6.00	5.21	3.74	1.80
	proton	2.41	2.52	2.27	1.54	1.63
	charged positive pion	0.526	0.747	0.878	0.520	1.69
	charged negative pion	0.536	0.856	0.852	0.492	1.74
	photon	2.72	4.48	4.42	3.41	1.65

Table 3.3. Comparison of neutron energy integral angular fluences above 20 MeV

	Name of code	Geant4 Shielding	PHITS	FLUKA 2021.2	FLUKA 4-2.2	
	Angle (degrees)	neutrons (>20 MeV)/sr/proton				max/min
Al	0	7.65	9.61	5.04	5.16	1.91
	15	1.04	0.943	0.904	0.889	1.17
	30	0.546	0.450	0.434	0.440	1.26
	45	0.376	0.288	0.266	0.277	1.41
	60	0.293	0.212	0.179	0.188	1.63
	90	0.199	0.109	0.0917	0.0992	2.17
	120	0.151	0.0606	0.0591	0.0663	2.56
	150	0.121	0.0438	0.0473	0.0537	2.77
Cu	0	6.22	8.34	4.40	4.49	1.89
	15	1.30	1.14	1.02	0.986	1.32
	30	0.778	0.605	0.551	0.554	1.41
	45	0.576	0.410	0.364	0.377	1.58
	60	0.473	0.310	0.260	0.273	1.82
	90	0.352	0.173	0.151	0.162	2.33
	120	0.282	0.104	0.107	0.116	2.64
	150	0.228	0.0771	0.0880	0.0961	2.96
Au	0	4.76	6.73	3.60	3.62	1.87
	15	1.69	1.54	1.27	3.62	0.47
	30	1.19	1.00	0.826	0.828	1.44
	45	0.964	0.751	0.613	0.632	1.57
	60	0.843	0.596	0.478	0.501	1.76
	90	0.703	0.370	0.323	0.343	2.18
	120	0.611	0.244	0.251	0.267	2.51
	150	0.513	0.186	0.215	0.228	2.76

Table 3.4. Comparison of proton energy integral angular fluences above 20 MeV

	Name of code	Geant4 Shielding	PHITS	FLUKA 2021.2	FLUKA 4-2.2	
	Angle (degrees)	protons (>20 MeV)/sr/proton				max/min
Al	0	1136	1261	1062	1054	1.20
	15	0.871	0.832	0.857	0.834	1.05
	30	0.334	0.335	0.347	0.345	1.04
	45	0.191	0.189	0.188	0.194	1.03
	60	0.133	0.123	0.112	0.117	1.19
	90	0.0767	0.0472	0.0438	0.0481	1.75
	120	0.0460	0.0210	0.0231	0.0265	2.19
	150	0.0219	0.0101	0.0128	0.0150	2.17
Cu	0	984	1257	972	931	1.35
	15	0.958	0.895	0.874	0.822	1.17
	30	0.407	0.390	0.390	0.380	1.07
	45	0.250	0.229	0.224	0.226	1.12
	60	0.186	0.152	0.139	0.144	1.34
	90	0.121	0.0632	0.0615	0.0657	1.98
	120	0.0791	0.0296	0.0353	0.0384	2.67
	150	0.0383	0.0140	0.0196	0.0214	2.75
Au	0	652	1395	614	544	2.57
	15	0.950	0.921	0.846	0.758	1.25
	30	0.480	0.466	0.425	0.402	1.20
	45	0.328	0.295	0.256	0.253	1.30
	60	0.268	0.203	0.165	0.167	1.62
	90	0.204	0.0921	0.0798	0.0828	2.55
	120	0.148	0.0446	0.0480	0.0499	3.32
	150	0.0751	0.0206	0.0263	0.0271	3.65

Table 3.5. Comparison of charged positive pion energy integral angular fluences above 20 MeV

	Name of code	Geant4 Shielding	PHITS	FLUKA 2021.2	FLUKA 4-2.2	
	Angle (degrees)	charged positive pions (>20 MeV)/sr/proton				max/min
Al	0	1.74	1.75	2.10	2.16	1.24
	15	0.778	0.638	0.759	0.760	1.22
	30	0.248	0.219	0.235	0.224	1.13
	45	0.0947	0.0938	0.101	0.0908	1.12
	60	0.0444	0.0497	0.0535	0.0458	1.21
	90	0.0157	0.0223	0.0220	0.0180	1.42
	120	0.00880	0.0133	0.0135	0.0106	1.53
	150	0.00583	0.00865	0.00917	0.00714	1.57
Cu	0	1.45	1.53	1.92	2.02	1.39
	15	0.748	0.598	0.733	0.725	1.25
	30	0.251	0.214	0.232	0.213	1.18
	45	0.0979	0.0950	0.102	0.0873	1.17
	60	0.0469	0.0517	0.0544	0.0444	1.23
	90	0.0169	0.0239	0.0229	0.0177	1.42
	120	0.00953	0.0143	0.0142	0.0104	1.51
	150	0.00630	0.00911	0.00960	0.00686	1.53
Au	0	1.00	1.14	1.61	1.84	1.85
	15	0.625	0.489	0.673	0.642	1.28
	30	0.225	0.189	0.217	0.190	1.19
	45	0.0921	0.0885	0.0971	0.0803	1.21
	60	0.0458	0.0502	0.0523	0.0419	1.25
	90	0.0185	0.0241	0.0223	0.0168	1.43
	120	0.0114	0.0146	0.0139	0.00982	1.49
	150	0.00769	0.00921	0.00923	0.00623	1.48

Table 3.6. Comparison of charged negative pion energy integral angular fluences above 20 MeV

	Name of code	Geant4 Shielding	PHITS	FLUKA 2021.2	FLUKA 4-2.2	
	Angle (degrees)	charged negative pions (>20 MeV)/sr/proton				max/min
Al	0	1.40	1.37	1.33	1.40	1.06
	15	0.671	0.539	0.596	0.600	1.24
	30	0.212	0.193	0.210	0.197	1.09
	45	0.0802	0.0854	0.0943	0.0827	1.18
	60	0.0374	0.0460	0.0500	0.0419	1.34
	90	0.0135	0.0208	0.0204	0.0163	1.54
	120	0.00785	0.0124	0.0123	0.00948	1.57
	150	0.00529	0.00804	0.00814	0.00614	1.54
Cu	0	1.26	1.29	1.21	1.36	1.07
	15	0.687	0.539	0.593	0.593	1.27
	30	0.225	0.204	0.217	0.196	1.15
	45	0.0873	0.0944	0.0994	0.0835	1.19
	60	0.0413	0.0530	0.0534	0.0427	1.29
	90	0.0155	0.0254	0.0222	0.0167	1.63
	120	0.00917	0.0153	0.0134	0.00960	1.67
	150	0.00618	0.00980	0.00888	0.00604	1.62
Au	0	0.980	1.09	1.05	1.28	1.31
	15	0.648	0.490	0.586	0.568	1.32
	30	0.227	0.205	0.225	0.194	1.17
	45	0.0904	0.104	0.106	0.0854	1.24
	60	0.0448	0.0630	0.0578	0.0450	1.41
	90	0.0191	0.0326	0.0243	0.0177	1.84
	120	0.0126	0.0203	0.0146	0.00990	2.05
	150	0.00909	0.0126	0.00935	0.00587	2.15

Table 3.7. Comparison of photon energy integral angular fluences above 20 MeV

	Name of code	Geant4 Shielding	PHITS	FLUKA 2021.2	FLUKA 4-2.2	
	Angle (degrees)	photons (>20 MeV)/sr/proton				max/min
Al	0	10.7	15.4	16.4	21.7	2.02
	15	2.52	2.26	2.53	2.98	1.32
	30	0.683	0.623	0.654	0.704	1.13
	45	0.296	0.306	0.314	0.320	1.08
	60	0.160	0.189	0.186	0.185	1.18
	90	0.0691	0.103	0.0924	0.0907	1.49
	120	0.0424	0.0714	0.0622	0.0612	1.68
	150	0.0316	0.0561	0.0486	0.0485	1.78
Cu	0	7.23	10.7	11.7	16.6	2.30
	15	4.54	4.13	4.65	5.74	1.39
	30	0.950	0.865	0.872	0.952	1.10
	45	0.333	0.354	0.340	0.338	1.06
	60	0.168	0.210	0.190	0.179	1.25
	90	0.0722	0.117	0.0933	0.0847	1.62
	120	0.0455	0.0829	0.0631	0.0569	1.82
	150	0.0342	0.0658	0.0494	0.0448	1.93
Au	0	2.10	2.94	3.57	5.57	2.66
	15	3.09	2.94	3.76	4.70	1.60
	30	1.37	1.32	1.41	1.57	1.19
	45	0.473	0.539	0.509	0.516	1.14
	60	0.211	0.288	0.239	0.225	1.37
	90	0.0847	0.147	0.0979	0.0856	1.74
	120	0.0563	0.103	0.0627	0.0532	1.83
	150	0.0404	0.0724	0.0426	0.0359	2.01

3.7. Summary and Conclusions

From the comparisons shown above, we can summarize the following results:

(1) The differences in the energy integral angular distribution above 20 MeV between the codes are remarkable at 0 degrees and above 90 degrees for neutrons and protons from the Al, Cu, and Au targets.

(2) The differences of energy integral angular distribution above 20 MeV between the codes for charged positive pions, charged negative pions and photons are smaller than those for neutrons and protons but show a similar tendency to increase at 0 degrees and above 90 degrees.

(3) Similar tendencies were observed for the differences in the particle spectra. The differences in the spectra are smaller at 15, 30, and 60 degrees.

The following actions are proposed for the next meeting:

(1) The developers of each code should check the model considering the results of this inter-comparison and send revised results to the organizer until the next meeting.

(2) It is desirable to include the results of MCNP6 and MARS

3.8. List of references

H. Hirayama and T. Sanami, “Intercomparison of particle production”, Proceedings of 14th Specialists’ workshop on Shielding aspects of Accelerators and Targets, and Irradiation Facilities (SATIF-14), Gyeongju, Korea, October 30 - November 2, 2018, OECD NEA/NSC/R(2021)2, pp.222-278.

4. The Shielding Integral Benchmark Archive Database (SINBAD) Task Force

Thomas Miller[1], Oliver Buss*[2], Michael Fleming[2]

[1]Oak Ridge National Laboratory,Spallation Neutron Source, Second Target Station Project, Oak Ridge, Tennessee, USA

[2]OECD Nuclear Energy Agency, Paris, France

*oliver.buss@oecd-nea.org

The management of the Shielding Integral Benchmark Archive Database (SINBAD) is now maintained by a devoted Task Force under the auspice of the OECD NEA Expert Group on Physics of Reactor Systems (EGPRS). This new SINBAD Task Force (TF) was mandated in February 2021 and established in Q1 2022 to oversee the future development of SINBAD, which is consistent with the strategy of the Nuclear Energy Agency (NEA) to continuously improve data available from the Data Bank. The TF consist of shielding experts, experimentalists, and benchmark evaluators from the EGPRS and other invited experts and is to operate on a three-year renewable mandate.

The proposed aim of the TF is to maintain and initiate the process of modernizing SINBAD benchmark entries. There are two major factors that led to the EGPRS establishing the TF. First, the international community recognizes that the rate of SINBAD development does not match the importance of the shielding benchmark topic. The TF will reinvigorate benchmark creation with a sustainable target of 3-4 new evaluations per year. The second motivating factor is to modernize the database while building upon previous work, which includes all entries currently in SINBAD and quality reviews provided over the years by several SINBAD evaluators. In this modernization effort the TF will operate like a technical review group and will strive to achieve a similar level of quality as the International Criticality Safety Benchmark Evaluation Project (ICSBEP) and the International Reactor Physics Experiment (IRPhE) Project. The EGPRS and the TF members have defined several goals for the TF, which include: avoid loss or removal of any existing information from the database, involve the nuclear data community and other user communities, include additional supplemental data (e.g. CAD files, simulation code inputs and outputs), and produce a single, peer-reviewed and approved summary document for each evaluation that follows the SINBAD evaluation guide approved by the Expert Group. The SINBAD database is now maintained in a GitLab environment hosted by the NEA, which ensures complete traceability of its update cycles.

There are a few conditions for reporting and operating that the EGPRS has specified for the TF. Otherwise, the TF has the freedom to define an optimum update process for SINBAD. The TF is required to report their progress each year at the annual EGPRS meeting. The EGPRS allotted a three-year period for the TF, which started in March 2021 and will end in March 2024. After those three years the EGPRS will review the progress of the TF and decide if it will be renewed.

If you or your colleagues have interest in participating in the SINBAD TF, please contact the WPRS Secretariat: wprs@oecd-nea.org .

5. MCNP6.2 benchmark calculations against measurements of neutrons produced in the spallation targets

Yurdunaz Celik[1*], Yosuke Iwamoto[2], Alexey Stankovskiy[1], Gert Van den Eynde[1]
[1]SCK CEN, Belgian Nuclear Research Institute, Boeretang 200, 2400 Mol, Belgium
[2]Japan Atomic Energy Agency, Tokai, Ibaraki, Japan
[*]ycelik@sckcen.be

Particle transport calculations play a key role in designing the MYRRHA target and subcritical reactor, and in order to guarantee high quality of the calculation results, code benchmarking against experiments is important and inevitable. In this work, the MCNP6.2 code was used to evaluate the impact of the nuclear data libraries and physics models in determining the neutron yield from the thick spallation targets and reaction rates in the shielding material. Two experiments were selected from the SINBAD database focusing on the MYRRHA target and proton beam energy similarities (i.e., lead target and 600 MeV proton beam energy). A third experiment was taken from literature. The compared quantities are the neutron yields and fluxes produced in thick lead targets, transmitted neutron fluxes generated from the W target and reaction rates in the shielding material.

Our study shows that MCNP6.2 results obtained with different physics models agree well with the experimental data in terms of neutron yield magnitudes and anisotropies in the scattering angles. Reaction rate calculations reveal that discrepancies occur due to neutron production or activation cross sections used to convert transmitted neutron fluxes through the concrete shield layers, in which activation foils were located for the measurements, rather than the physic models employed in the transport calculations.

5.1. Introduction

MYRRHA (Multi-purpose hYbrid Research Reactor for High-tech Applications) is a multipurpose research facility currently being developed at SCK CEN (Aït Abderrahim et al., 2021). It is based on the ADS (Accelerator Driven System) concept where a proton accelerator, a spallation target and a subcritical reactor are coupled. Lead-bismuth eutectic (LBE) has been selected as coolant and as spallation source in which the proton beam coming from the accelerator is converted into neutrons which sustain the fission reaction in the subcritical core surrounding the spallation target. The neutron fluxes produced in the spallation target by incident protons impact the entire ADS design. Therefore it is important to test the performance of Monte Carlo radiation transport codes such as MCNP6.2 (Werner, 2017) in terms of fast neutron emissions during spallation reactions in a thick target.

In this work, benchmark calculations were performed to compare with the experimental double differential neutron yields and fast neutron fluxes from a Pb target hit by 500 MeV (Meigo et al.,1999) and 590 MeV (Cierjacks et al., 1981) proton beams, respectively. Furthermore, reaction rate measurements obtained with the transmitted neutron flux, which is generated from tungsten target hit by 500 MeV protons and transmitted through concrete shield (Nakao et al., 2004), were also used for the comparison. The neutron flux and reaction rate experiments were selected from the reactor related SINBAD database (SINBAD).

The calculations were carried out with the MCNP6.2 radiation transport code (Werner, 2017) considering either solely physics models or a combination of physics models with proton and neutron-induced evaluated cross section libraries. This work is an extension of

the benchmark study (Iwamoto et al., 2022) performed with the PHITS radiation transport code and JENDL-4.0/HE proton and neutron induced cross section library.

5.2. Methodology

This work focuses on the use of MCNP6.2 radiation transport code, which is extensively validated against experimental data for the prediction of neutron yields from proton interactions in light or heavy target materials (Tayama et al., 2002; Itoga et al., 2005; Oh et al., 2011). The MCNP6.2 code possesses physics models to describe various stages of the spallation reactions: Intra-Nuclear Cascade (INC), pre-equilibrium stage, and de-excitation, which may proceed through evaporation or fission. Each reaction stage is described by different physics models as shown in Figure 5.1.

The intranuclear cascade model INCL4 (Boudard et al., 2002) does not consider a pre-equilibrium stage after the cascade and can be directly combined with either ABLA (Gaimard et al., 1991) or Dresner (1981) evaporation models in the same way as Bertini (1963) and ISABEL (Yariv, 1981) INC models that presume MPM pre-equilibrium stage. CEM03.03 (Mashnik et al., 2012) has its own built-in pre-equilibrium and de-excitation models. It is the default physics model of MCNP6.2. This choice was made based on the extensive validation efforts demonstrating key improvements (Mashnik, 2011; Mashnik et al. 2008) compared to the Bertini/Dresner combination, which was the default model in the preceding MCNPX 2.7.0 version (Pelowitz, 2011). For the calculations reported in this work, all physics models were tested except the Dresner evaporation model which gives small discrepancies at the evaporation region compared with the ABLA model. Therefore, only ABLA evaporation model was combined with Bertini, ISABEL and INCL4 models.

Figure 5.1. MCNP6.2 physics models (Werner, 2017).

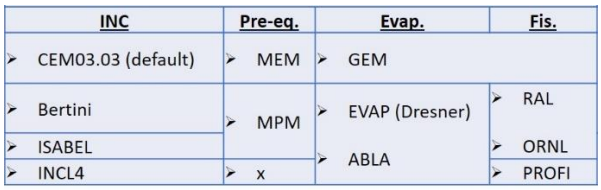

The user has several options to determine the likelihood of interaction between particles by using only physics models, only the cross-section library or a Mix & Match strategy of data tables and physics models for the missing data and above the maximum energy in the data tables throughout a problem. Given the fact that the investigated beam energies in this work are above the evaluated nuclear data tables, all three options were used for the simulations.

There are numerous general purpose nuclear data libraries available worldwide: the largest nuclear data projects are JEFF (OECD/NEA) (Plompen et al., 2020), JENDL (Japan) (Shibata et al., 2011), ENDF/B (USA) (Chadwick et al. 2006) and TENDL (Europe) (Koning et al., 2019). The following proton induced nuclear data files for lead and tungsten isotopes from three nuclear data libraries have been used in this work: JENDL-4.0/HE, TENDL-2017 and ENDF/B-VII.0. All three libraries have proton data up to 200 MeV for Pb and W isotopes, except the ENDF/B-VII.0, which has data up to 150 MeV for $^{182\text{-}186}$W and no data for ^{180}W. Since the selected experiments also have a scattering environment with collimator or shielding material besides the target material, neutron induced cross section libraries (i.e. JEFF-3.1.2, JEFF-3.3, ENDF/B-VII.1 and ENDF/B-VIII.0) were also tested.

5.3. Calculations and Results

5.3.1. Double differential neutron yields

The first investigated experiment was performed at KEK with a 20 cm thick lead target in a series of double differential neutron production cross section measurements (Meigo et al.,1999). A schematic view of the experimental arrangement is shown in Figure 5.2-left. The lead spallation target was bombarded by the 500 MeV proton beam. The detectors used for the neutron spectra measurements were placed at angles of 30°, 60°, 90°, 120° and 150° with respect to the beam axis and at a common distance of 1 m from the centre of the target. At the angle of 15°, the detector was located 1.5 m from the target. The target had a form of a rectangular parallelepiped with the dimensions of 15 cm x 15 cm x 20 cm. The MCNP6.2 model of the experimental arrangement with the spherical detectors have a radius of 1 m is also shown in Figure 5.2-right. The range of a polar angle was ± 1° for each angle.

Figure 5.2. The Illustration of the experimental arrangement (Meigo et al.,1999) (left) and the model used for the calculations (right).

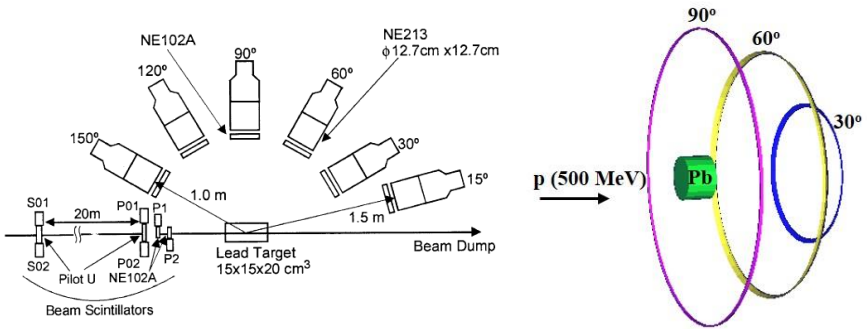

Since numerical experimental data was not presented in Meigo et al. (1999), a graph digitizer was used to extract the data from the graph image. The comparison of the experimental and calculated neutron fluxes obtained with 500 MeV proton beam hitting on a Pb target is shown in Figure 5.3. The calculations were performed using JENDL-4.0/HE nuclear data library for neutron and proton interactions up to 200 MeV. Above 200 MeV, physics models were used. It can be seen that the predictions of the different physics models show reasonable estimates of double differential (with respect to angle and energy) neutron yields compared to the experiments.

The neutron yield spectral profiles at three different scattering angles have the general features of the angular dependent neutron production. That is, up to ~ 20 MeV, the neutron yield absolute values are still of about the same order and slightly decrease with increasing scattering angle. The neutron yields above the evaporation spectrum in the cascade energy range (> 20 MeV) are strongly angular-dependent and rapidly decrease with increasing energy. In other words, the neutron yield profiles have three different spectral shapes that have a broad peak around 1 MeV, then a rapid fall to about 20 MeV and a broad shoulder up to around 100 MeV. The calculation results predicted by the physics models capture such spectral characteristics well, even though there are slight differences between them.

The default model, i.e. CEM03.03, either overestimates or underestimates the neutron yields by 30% between 5 MeV –30 MeV and above 50 MeV at 90° scattering angle compared to those of the INCL/ABLA model, respectively. The obtained results with

Bertini/ABLA and ISABEL/ABLA are almost the same showing slight differences from the result of CEM03.03.

Large discrepancies between the calculations and the measured data are observed at lower energies (i.e. < 5 MeV) especially at 30° scattering angle, as shown in the left panel of Figure 5.3. To understand this behaviour, test calculations were performed using only physics models. It was observed that if, for example, only CEM03.03 model is used for the neutron interactions rather than the neutron induced nuclear data library (i.e. JENDL-4.0/HE), the results are lower by factor of 2 up to 2 MeV (see Figure 5.3-right). It can be concluded that the results obtained with the neutron induced nuclear data library are improving with increasing scattering angle, which is contrary to the case when only physics models are used, for which the results are improving with the decreasing scattering angle below neutron energy of 5 MeV. Above 5 MeV, physics models are prevailing to determine the neutron yield.

It was also determined that different neutron libraries (e.g. JENDL-4.0/HE, ENDF/V-VI, JEFF-3.3, ENDF/B-VIII.0 and JEFF-3.1.2) induce max. 15% relative difference compared to each other. Therefore, those results are not graphically presented.

Using different proton induced libraries (i.e. TENDL-2017, JENDL-4.0/HE and ENDF/B-VII) for the proton interactions also does not show a considerable impact neither on the flux profile nor in the absolute values. The relative difference between them is at maximum 5%.

Figure 5.3. Fast neutron yield distributions for 500 MeV protons on a 20 cm thick Pb target at three measuring angles. JENDL-4.0/HE was used for neutrons and protons up to 200 MeV, while physics models were used above 200 MeV (left).

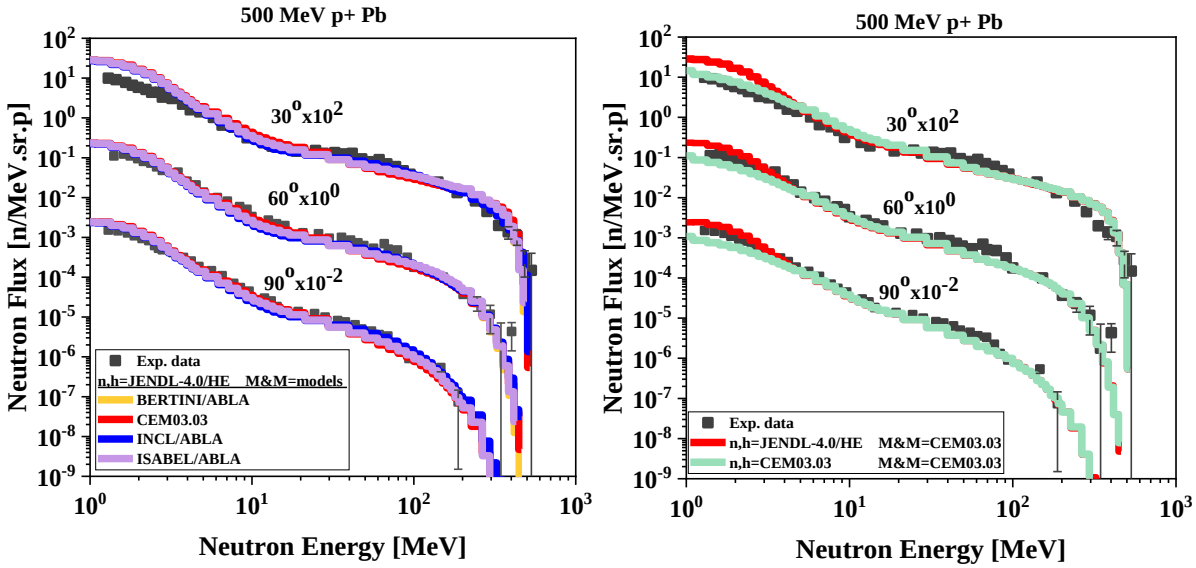

5.3.1. Fast neutron yield distribution

The second investigated experiment was performed at the SIN cyclotron (Cierjacks et al., 1981) to obtain angular neutron spectra resulting from 590-MeV protons hitting on a thick lead target. A 590 MeV proton beam of 2 cm diameter was focused onto a lead target. The target was composed of twelve cylindrical blocks, each 5 cm long and 10 cm in diameter, giving an overall length of 60 cm. Neutrons emitted from the target were measured at 30°,

90° and 150° at the exit of a ~1 m iron collimator. The experimental arrangement is illustrated in Figure 5.4. The MCNP6.2 model used for the calculations is described in (SINBAD).

Figure 5.4. The calculation geometry for the SIN experiment (SINBAD). Neutrons are generated by 590 MeV protons bombarding a thick lead target.

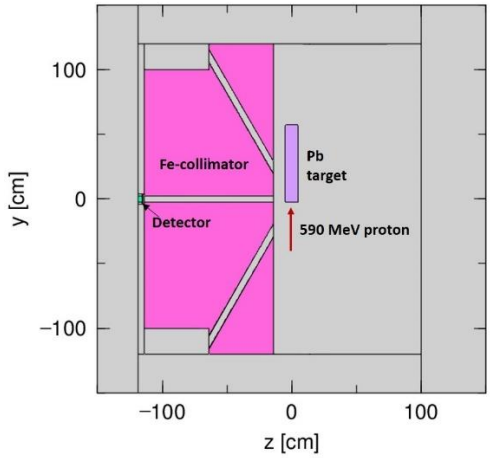

Figure 5.5-left shows the calculated and experimental fast neutron flux distributions for 590 MeV protons on a Pb target at 90° measuring angle. Several calculations were performed considering only CEM03.03 and INCL4/ABLA physics models for neutron and/or proton interactions, and in Mix & Match method when nuclear data libraries were used up to 200 MeV.

The neutron flux profile is seen to be very much alike with the neutron yield curves presented in the previous section and similar observations were made here as well. Namely, using a neutron induced library (i.e. JENDL-4.0/HE, shown in red colour) rather than a physics model (shown in blue colour) increases the neutron production above ~4 MeV, as shown in the left plot of Fig. 1.5. Again, a negligible impact on the results of using proton induced library up to 200 MeV can be observed.

The INCL4 model combined with the ABLA evaporation model (shown in blue colour) better predicts the evaporation neutrons dominating the energy range below 20 MeV as well as the cascade neutrons governing the spectral shape above 20 MeV compared to the CEM03.03 model shown in red colour.

To determine the impact of the neutron libraries, the neutron interactions in the target and collimator were modelled using the neutron evaluated libraries JEFF-3.1.2, JEFF-3.3, JENDL-4.0/HE, ENDF/B-VII.1, ENDF/B-VIII.0, as shown in the right panel of Figure 5.5. The CEM03.03 model was used for proton interactions as well as for neutron interactions in Mix & Match method for the isotopes with missing neutron data or beyond the maximum data energy. One can observe that discrepancies between the libraries occur due to the neutron data of iron used as a collimator and are more pronounced above 20 MeV. Comparing the neutron data libraries, the JEFF-3.3 library provides results closest to the experiment in terms of absolute values.

Figure 5.5. Fast neutron yield distributions for 590 MeV protons on a 60 cm thick Pb target at 90° measuring angle. Above 200 MeV, CEM03.03 physics model is used for neutron and proton interactions.

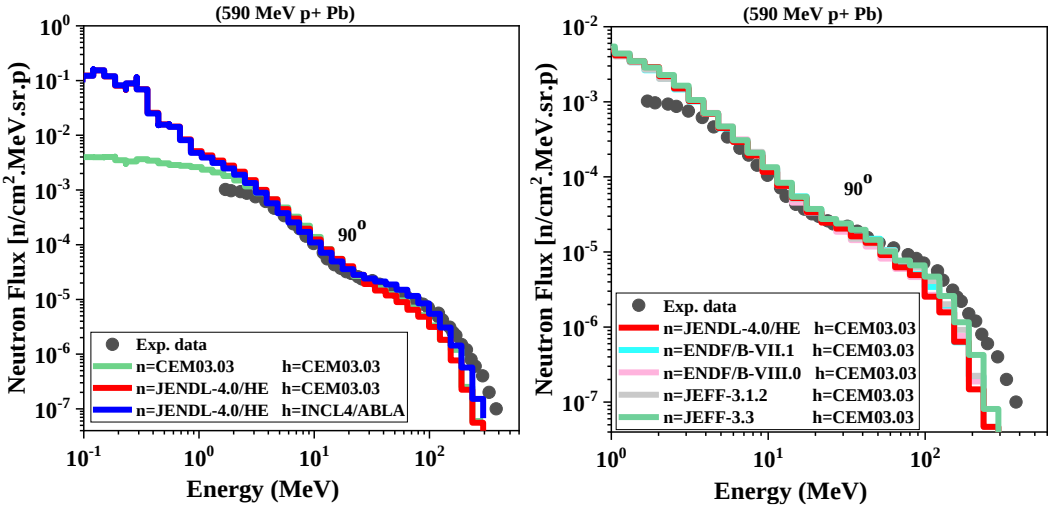

5.3.2. Reaction rate measurements

The third investigated experiment was performed at KENS spallation neutron source facility to check the accuracies of the transmission and activation calculation codes (Nakao et al., 2004). A high-energy neutron source was produced in the forward direction from a thick tungsten target bombarded by a 5 μA beam of 500 MeV protons and was scored in the irradiation room behind the ordinary concrete as shown in Figure 5.6. An ordinary concrete shield of 4 m thickness was located behind the open iron beam shutter and heavy concrete. Seven activation detectors of bismuth, aluminium, indium and gold were placed in slots every 40–80 cm in the concrete shield on the beam axis. A final detector was placed at the end of the concrete shield. The threshold energies of the detectors range from 0.34 MeV (^{115}In(n,n')^{115m}In) to ~54 MeV (^{209}Bi(n,8n)^{203}Bi).

From the analyses of the photon peak counts of each detector foil, the reaction rates of ^{209}Bi(n,xn)$^{210-x}$Bi (x=4-8), ^{27}Al(n,a)^{24}Na, ^{27}Al(n,x)^{22}Na, ^{27}Al(n,x)^{7}Be, ^{115}In(n,n')^{115m}ln and ^{197}Au(n,γ)^{198}Au were obtained.

Figure 5.6. Calculation geometry for the KENS experiment performed with 500 MeV protons bombarding a thick tungsten target.

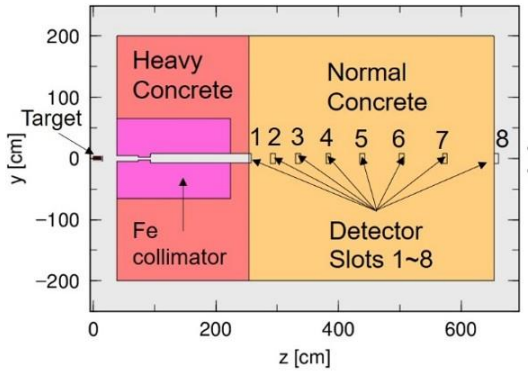

Figure 5.7 shows the transmitted neutron spectra in the slabs located in the standard concrete. The calculations were performed using JENDL-4.0/HE nuclear data library for neutron and proton interactions up to 200 MeV. Above 200 MeV, physics models were used.

Figure 5.7. Calculated neutron energy spectra in the concrete shield at each depth for the KENS experiment.

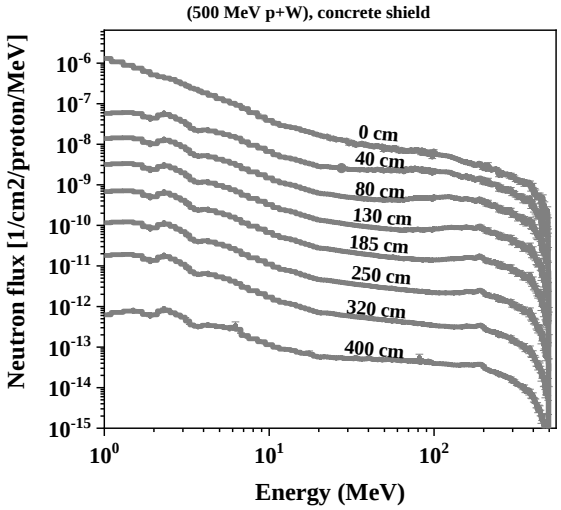

The cross sections for activation reactions involving different target nuclei in the ground and excited states were used as an energy-dependent response functions in MCNP6.2 to determine reaction rates but not for the transport calculations. For example, the ^{27}Al(n, α)^{24}Na reaction cross section was only used in an energy-dependent DE/DF card to modify the neutron flux scores in F4 tally.

The selected cross sections are compared in Figure 5.8 in order to choose the most appropriate for the final calculations. For ^{209}Bi(n, xn)$^{210-x}$Bi (x = 4–6) reactions, residual nuclide production cross sections were obtained from JENDL-4.0/HE and ENDF/B-VIII.0 libraries using the JANIS tool (JANIS). It should be noted that according to the ENDF-6 format specifications (Trkov et. al., 2018) the residual production cross sections are obtained as a product of total nonelastic reaction cross section (MF=3, MT=6) with residual nucleus yield from MF=6, MT=5. The neutron production cross sections (MF=3 with MT=37, MT=152 and MT=153 for (n,4n), (n,5n) and (n,6n), respectively) from IRDFF-II (IAEA) and ENDF/B-VI from Nunomiya (2002) for all ^{209}Bi(n, xn)$^{210-x}$Bi (x = 4-9) reactions were taken. For ^{27}Al(n, α)24Na, ^{115}In(n, n')^{115m}In and ^{197}Au(n,γ)^{198}Au reaction cross sections were taken from JANIS tool using MF=3, MT=107, MF=10, MT=4, and MF=3 , MT=102, respectively.

Figure 5.9 shows the reaction rate distribution in the concrete shield at each depth. The results were calculated with the reaction cross sections providing the estimates closest to the experiments. That is, the best experimental reaction rates were obtained using IRDFF-II for ^{27}Al, ^{115}In and ^{197}Au, while ENDF/B-VI* cross sections were employed for ^{209}Bi reactions. It is seen that the calculated results match with the experiments well enough, except for ^{197}Au.

Residual nuclide production cross section for ^{115}In(n, n')^{115m}In from JENDL/AD-2007 library, which has data up to 20 MeV, gives 23% higher ^{115m}In yield than the corresponding

cross section from IRDFF-II, which contains data up to 60 MeV. As shown in the top-middle plot of Figure 5.8, JENDL/AD-2007 has a peak at 10 MeV, at which neutron fluxes are also higher (see Figure 5.7). TENDL-2019 gives a ~2% higher ^{24}Na production compared to IRDFF-II. The neutron capture rates for ^{198}Au production are almost equal with all the considered cross sections as seen in Figure 5.8-top right. To summarize, the MCNP6.2 calculations predict the experimental data at 7th slot within a factor of 2 for Au as a largest discrepancy, while the accuracy of the other calculated reaction rates is 2% - 40% .

Figure 5.8. Cross sections.

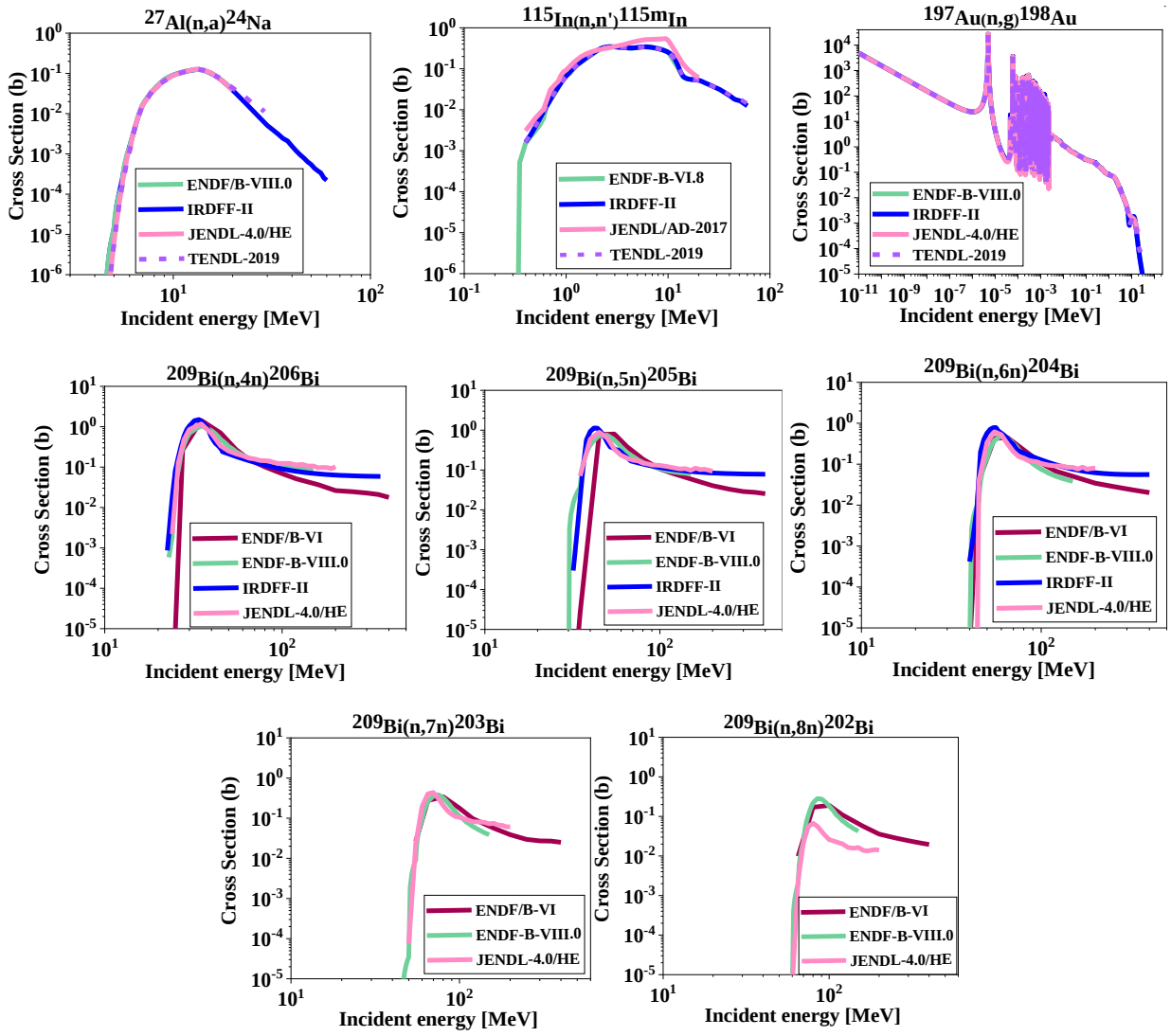

Figure 5.9. Reaction rate at each depth in concrete shields of the KENS experiment.

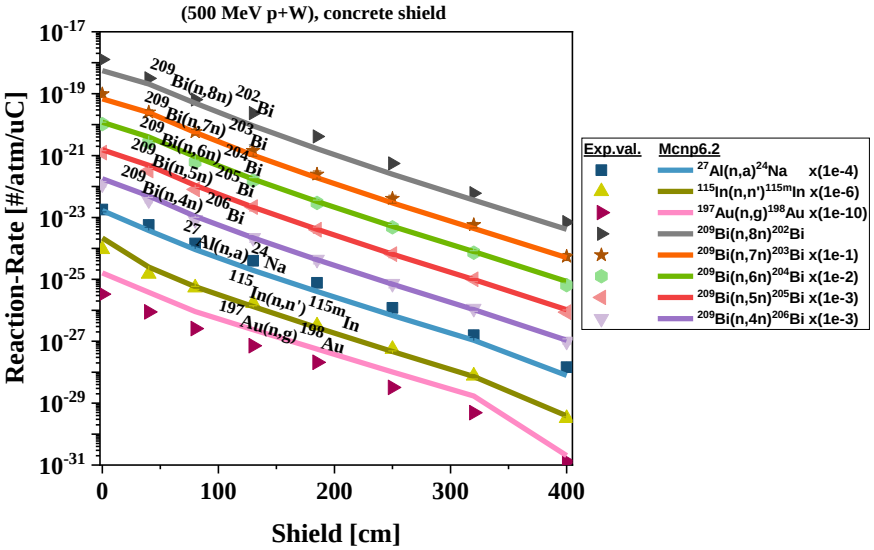

5.4. Conclusions

MCNP6.2 benchmark calculations were performed for the following three experimental cases: 1) angular and energy dependent neutron yields produced with 500 MeV protons hitting a thick lead target, 2) fast neutron fluxes produced with 590 MeV protons hitting a thick lead target, 3) reaction rates using transmitted neutron fluxes produced with 500 MeV protons hitting a tungsten target.

The calculation results of double differential neutron yields and fast neutron fluxes from thick Pb targets demonstrate that quality of the physics models is a prevailing factor above 5 MeV. Comparison of the calculated and measured data in the range 1 - 5 MeV indicates that neutron induced nuclear data improve predictions with increasing scattering angle, while physics models behave exactly opposite. This statement needs further confirmation using additional experimental data at backward angles with respect to the proton beam direction.

The calculation results predicted by the physics models adequately reproduce the spectral characteristics of the differential neutron yields at all scattering angles. Among the investigated physics models, INCL4 simulates well the experimental neutron flux measured at a 90° scattering angle from the lead target compared to CEM03.03, which is the default model of MCNP6.2.

The impact of the proton induced libraries used up to 200 MeV is negligible for all cases. The closest results to the experimental flux data in terms of absolute values were obtained with JEFF-3.3 neutron library beyond 20 MeV due to high sensitivity to the neutron data for iron isotopes.

It was observed that the calculated and experimental values for the reaction rates agree within a factor of 2 for Au at the 7th slot as a largest discrepancy, which requires more reliable experimental data. A good agreement is observed for the experimental and calculated values by 2% - 40% for the other experimental reaction rates at the 7th slot.

5.5. List of references

Aït Abderrahim H. and Giot M., (2021), "The Accelerator Driven Systems, a 21st Century Option for Closing Nuclear Fuel Cycles and Transmuting Minor Actinides," Sustainability, 13, 12643.

Werner C. J. (editor), (2017), "MCNP Users Manual - Code Version 6.2, " LA-UR-17-29981, Rev. 0, Los Alamos National Security, LLC.

Meigo, S., et al. (1999), "Measurements of neutron spectra produced from a thick lead target bombarded with 0.5- and 1.5-GeV protons", Nuclear Instruments and Methods in Physics Research. A 431, pg. 521-530.

Cierjacks, S., et al. (1981), "High energy particle spectra from spallation targets", Proceedings of the 5th Meeting of the International Collaboration on Advanced Neutron Sources, Jülich, June 22-26.

Nakao, N., et al. (2004), "KENS shielding experiment (1) - measurement of neutron attenuation through 4 m concrete shield using a high energy neutron irradiation room", Journal of Nuclear Science and Technology, 41:sup4, 22-25.

SINBAD, OECD/NEA Databank, NEA-1552/15, https://www.oecd-nea.org/science/wprs/shielding/sinbad/

Iwamoto Y., et al. (2022), "Benchmark Study of Particle and Heavy-Ion Transport Code System using Shielding Integral Benchmark Archive and Database for Accelerator-Shielding Experiments," Journal of Nuclear Science and Technology, 59, 5, 665.

Tayama R., et al. (2002), "Benchmark calculations of neutron yields and dose equivalent from thick iron target for 52–256 MeV protons," Nuc. Eng. and Des. 213, 119–131.

Itoga T., et al. (2005), "Neutron Production from Thin Target of Carbon and Iron by 70 MeV Protons, " JAERI-Conf-2005-003, Japan.

Oh J., et al. (2011), "Comparison of the FLUKA, MCNPX, and PHITS Codes in Yield Calculation of Secondary Particles Produced by Intermediate Energy Proton Beam," Progress in Nuclear Science and Technology, Vol. 1, p.85-88.

Boudard A., et al. (2002), "Intranuclear cascade model for a comprehensive description of spallation reaction data," Phys. Rev. C 66, 044615.

Gaimard J. J. and Schmidt K. H., (1991), "A reexamination of the abrasion ablation model for the description of the nuclear fragmentation reaction," Nucl. Phys. A 531, pp. 709–745.

Dresner L., (1981), "EVAP-A Fortran Program for Calculating the Evaporation of Various Particles from Excited Compound Nuclei," Oak Ridge National Laboratory report ORNL-TM-7882.

Bertini H. W., (1963), "Low-Energy Intranuclear Cascade Calculation," Phys. Rev 131, 1801.

Yariv Y. and Fraenkel Z., (1981), "Inclusive Cascade Calculation of High Energy Heavy Ion Collisions: Effect of Interactions between Cascade Particles," Phys Rev C 24, 488.

Mashnik S. G. and Sierk A. J., (2012), "CEM03.03 User Manual," Los Alamos National Laboratory report LA-UR-12-01364.

Mashnik S., (2011), "Validation and Verification of MCNP6 Against High-Energy Experimental Data and Calculations by Other Codes. I. The CEM Testing Primer," LA-UR-11-05129.

Mashnik S. G., et al. (2008), "CEM03.03 and LAQGSM03.03 Event Generators for the MCNP6, MCNPX, and MARS15 Transport Codes," LANL Report LA-UR- 08-2931.

Pelowitz D. B., et al. (2011), "MCNPX 2.7.0 Extensions, LA-UR-11-02295.

Plompen A. J. M., et al. (2020), "The Joint Evaluated Fission and Fusion Nuclear Data Library," The European Physical Journal A, 56, 181.

Shibata K., et al. (2011), "JENDL-4.0: A New Library for Nuclear Science and Engineering," Journal of Nuclear Science and Technology, 48,1, 1.

Chadwick M. B., et al. (2006), "ENDF/B-VII.0: Next Generation Evaluated Nuclear Data Library for Nuclear Science and Technology, " Nucl. Data Sheets, 107, 2931.

Koning A. J., et al. (2019), "TENDL: Complete Nuclear Data Library for Innovative Nuclear Science and Technology," Nuclear Data Sheets, 155, 1.

Trkov A, et al. (2020), "IRDFF-II: a new neutron metrology library, " Special Issue Nucl Data Sheets, 163:1–108.

JANIS, Available from: https://www- nds.iaea.org/exfor/endf.htm

Trkov A., et al. (2018), "ENDF-6 Formats Manual," CSEWG Document ENDF-102, Report BNL-203218-2018-INRE, SVN Commit: Revision 215.

IAEA Nuclear data services, ENDF-Archive, Available from: https://www-nds.iaea.org/exfor/endf.htm

Nunomiya T, et al. (2002), "Experimental data of deep-penetration neutrons through a concrete and iron shield at the ISIS spallation neutron source facility using an 800-MeV proton beam," KEK Report. p. 2001–2024.

5.6. List of abbreviations and acronyms

MYRRHA	Multi-purpose hYbrid Research Reactor for High-tech Applications
SCK CEN	Belgium Nuclear Research Center
SINBAD	Shielding Integral Benchmark Archive and Database
MCNP	Monte Carlo N-Particle® Code
PHITS	Particle and Heavy Ion Transport Code System
JENDL	Japanese Evaluated Nuclear Data Library
INC	Intra-Nuclear Cascade
INCL4	The Liège Intranuclear Cascade Model
CEM	Cascade Exciton Model
MPM	Multistage Pre-equilibrium Model
MEM	Modified Pre-equilibrium Model
GEM	Generalized Evaporation Model
JEFF	The Joint Evaluated Fission and Fusion (JEFF) Nuclear Data Library
JENDL	Japanese Evaluated Nuclear Data Library
ENDF/B	Evaluated Nuclear Data File Library
TENDL	TALYS Evaluated Nuclear Data Library

IRDFF-II International Reactor Dosimetry and Fusion File

6. Simulation studies of a pion production target for the Mu2e-II experiment

Anna Ferrari[1], Michael MacKenzie[2], Stefan E. Müller[1*], Vitaly Pronskikh[3], Reuven Rachamin[1] for the Radiation working group of the Mu2e-II Collaboration

[1]Helmholtz-Zentrum Dresden-Rossendorf, 01328 Dresden, Germany
[2]Northwestern University, Evanston, Illinois 60208, USA
[3]Fermi National Accelerator Laboratory, Batavia, Illinois 60510, USA
[*]Stefan.Mueller@hzdr.de

The Mu2e experiment, which is currently under construction at the Fermi National Accelerator Laboratory (FNAL) near Chicago, will search for the neutrinoless conversion of muons into electrons in the field of an aluminum nucleus with a sensitivity four orders of magnitude better than previous experiments. This process, which violates charged lepton flavor, is highly suppressed in the Standard Model and therefore undetectable. However, scenarios for physics beyond the Standard Model predict small but observable rates.

An extension of the Mu2e experiment making use of the PIP-II accelerator upgrade at FNAL is currently being studied. The Mu2e-II experiment aims to improve the sensitivity by at least a factor of 10 compared to Mu2e. To achieve this, it will utilize an 800 MeV proton beam with a beam power of 100 kW hitting a production target to produce the required amount of pions and muons. This high beam intensity requires a substantially more advanced target design with respect to Mu2e.

We will present simulation studies for several target designs. In particular, we will compare results for energy deposition, radiation damage and particle yields for both the targets and the surrounding materials using the MARS15, FLUKA2021 and Geant4 particle transport and reaction code packages.

6.1. Motivation

In our present understanding, the Standard Model of particle physics (SM) contains mixing of quarks via the CKM-matrix (Cabibbo, 1963; Kobayashi, Maskawa, 1973) and transitions between charged and neutral leptons of the same flavor. In addition, oscillations of neutrinos have been observed, introducing a violation of lepton flavor in the neutral lepton sector. Lepton flavor violation (LFV) in the charged lepton sector has so far never been observed. The Mu2e experiment, which is currently under construction at the Fermi National Accelerator Laboratory (FNAL) near Chicago, will search for the neutrinoless conversion of a muon into an electron in the Coulomb field of a nucleus ($\mu N \rightarrow eN$) normalized to all muon capture reactions with a projected upper limit of 6×10^{-17} (90% CL) (Bartoszek; 2015). This will be a sensitivity four orders of magnitude better than previous experiments, e.g. the SINDRUM-II experiment at the Paul-Scherrer Institut in Switzerland, which studied the process $\mu Au \rightarrow eAu$, reaching an upper limit for muon-to-electron-conversion on gold nuclei of $BR(\mu Au \rightarrow eAu) < 7\times10^{-13}$ (90% CL) (Bertl; 2006). The Standard Model predictions of charged lepton flavor violation (CLFV) is on the order of 10^{-54} via neutrino mixing (de Gouvêa; 2013), but possible extensions of the Standard Model like leptoquarks, heavy neutrinos or Supersymmetry predict values up to 10^{-14} (Bartoszek; 2015), well within reach of the anticipated sensitivity of the Mu2e experiment.

6.2. The Mu2e/Mu2e-II experiments

The Mu2e experiment (Bartoszek; 2015, Bernstein; 2019) will search for CLFV in the process ($\mu^- + Al \rightarrow e^- + Al$). The stopped muons have a lifetime of 864 ns in the 1s-orbital of the Al nucleus, where about 60% of the muons undergo the muon capture reaction and 40% decay in orbit with a Michel spectrum of the decay electron rapidly decreasing above an energy of half of the muon mass. The signal for muon-to-electron conversion would give a single mono-energetic electron with an energy close to the muon mass E_e=104.973 MeV (Czarnecki; 2011). The number of signal conversion-electron candidates will be normalized to the number of muon captures on aluminum in the same running period.

Figure 6.1 shows a sketch of the principal elements of the Mu2e experiment. The muons are obtained from an 8 GeV pulsed proton beam with a time-averaged power of 7.3 kW hitting a pion production target made from tungsten. A graded solenoidal magnetic field around the production target guides the pions towards an s-shaped transport solenoid (TS), in which the pions decay into muons. Inside the TS, absorber foils remove anti-protons and collimators select low-momentum negatively-charged muons. These muons then hit a stopping target made out of aluminum foils, where they either decay or undergo a capture reaction on the aluminum nuclei, or potentially undergo a CLFV conversion to a 105 MeV conversion electron. This conversion electron is then detected by a tracking detector and a calorimeter.

Figure 6.1. The Mu2e experiment

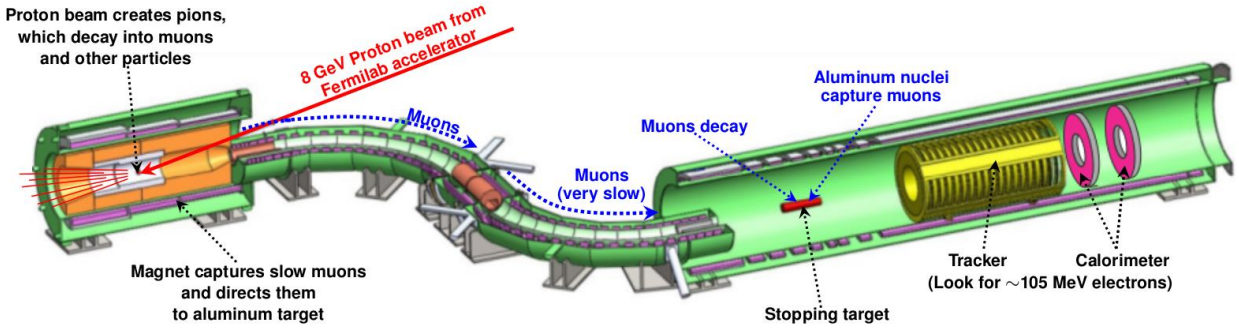

Source: Modified from https://mu2e.fnal.gov/images_v2/mu2edisk.jpg (Credit: Symmetry Magazine, used with permission)

While the Mu2e experiment is currently under construction at FNAL (with physics data taking starting in 2026), a possible upgrade is discussed with the aim to improve the sensitivity to $\mu \rightarrow e$ conversion by at least one order of magnitude (Byrum, 2022). This Mu2e-II experiment will make use of the more powerful proton source constructed at FNAL, which will deliver 100 kW of 800 MeV protons to the experiment (to be compared with 7.3 kW of 8 GeV protons at Mu2e), increasing the number of protons per second by two orders of magnitude with respect to the current Mu2e design.

The higher beam intensity for Mu2e-II requires extensive simulation studies for radiation and particle yields in the pion production target region, especially since ideally one would like to reuse as much as possible the existing shielding infrastructure.

6.3. Production Target designs

The initial design for Mu2e's pion production target was a simple cylindrical tungsten rod with 16 cm length and 0.315 cm radius, held in place by a sophisticated holder structure because the incoming beam is at an angle of 14° with respect to the production solenoid axis. However, since a fraction of about 10% of the 7.3 kW proton beam power is deposited into the target, a more sophisticated design was needed to allow for sufficient radiative cooling to reduce the temperature and the thermal stress of the target, such that it survives a full year of Mu2e running before being replaced. After several iterations, a final design was chosen which preserves the number of muons per proton-on-target (POT) while increasing the capability to radiate away the energy by attaching fin-like structures to the central rod (Figure 6.2, Left). This target has now been constructed and assembled at FNAL (Figure 6.2, Right).

Figure 6.2 The Mu2e pion production target

Left: Mu2e pion production target as modeled with Mu2e's offline framework (https://github.com/Mu2e/Offline/)
Right: Mu2e pion production target assembled at FNAL
Source: Mu2e collaboration, used with permission

Due to the higher proton beam intensity, Mu2e-II needs a pion production target which involves active cooling. The current target designs are based on a conveyor idea in which carbon or tungsten spheres are circulated to and from the proton beam at a speed of about 10 cm/s (Pronskikh, 2022). Figure 6.3 shows a design with tungsten spheres of 0.5 cm radius modeled with the MARS15 radiation transport and interaction program (Mokhov, 2007; Mokhov, 2017; Mokhov, 2022; Tropin, 2022). For this tungsten design, only about 9 spheres are in the proton beam trajectory at the same time, spending roughly 1 s in the beam each. In Figure 6.4, a design using carbon spheres of 0.6 cm radius is depicted, modeled with the FLUKA radiation transport and interaction program (Ferrari, 2005; Böhlen, 2014, Vlachoudis, 2009). In order to maintain the pion yield, the proton beam needs to pass through 28 carbon spheres in total due to the lower density of the carbon target material respect to tungsten. Along the path, the 800 MeV protons get deflected by the magnetic field in the production solenoid, and the position of the carbon spheres needs to follow the proton trajectory in order to make full use of the proton beam if the current magnetic field configuration for the Mu2e experiment is kept.

Figure 6.3. The Mu2e-II production target design using tungsten spheres

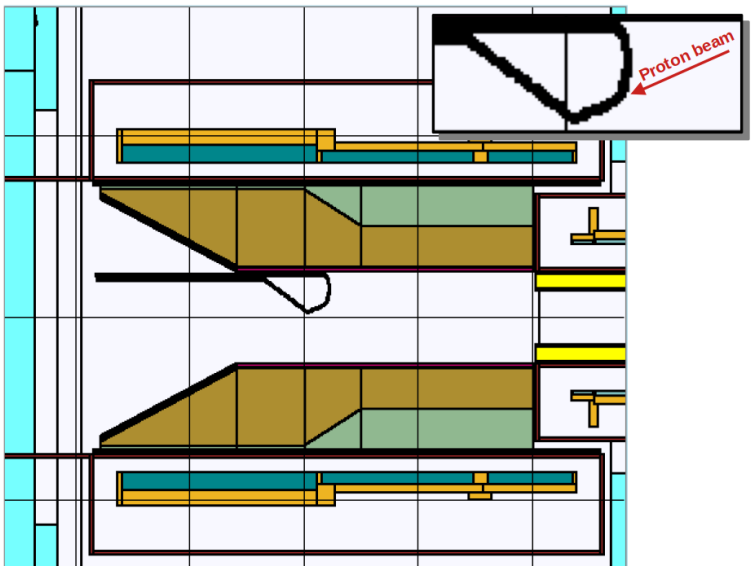

Note: The conveyor target design with tungsten spheres modeled with the MARS15 radiation transport and interaction package. The inset shows where the proton beam hits the spheres.

Figure 6.4. The Mu2e-II production target design using carbon spheres

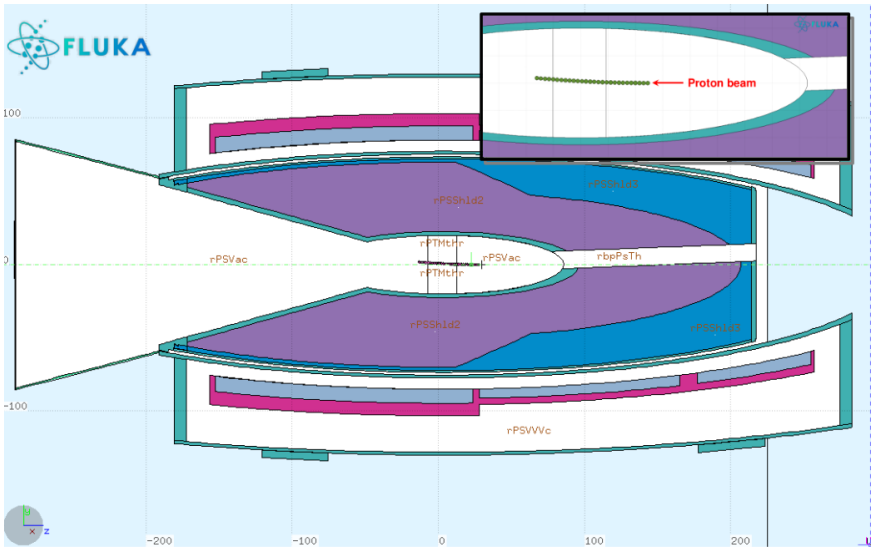

Note: The conveyor target design with carbon spheres modeled with the FLUKA radiation transport and interaction package. The figure is depicted in the plane of deflection of the proton trajectory by the magnetic field. The inset shows where the proton beam hits the spheres.

6.4. Simulation studies using the Mu2e-II production target designs

The two Mu2e-II production target designs were implemented with FLUKA2021[1] (Ferrari, 2005; Böhlen, 2014; Ferrari, 2022; Sala, 2022), MARS15 (Mokhov, 2007; Mokhov, 2017; Mokhov, 2022; Tropin, 2022) and the Mu2e Offline framework which is

[1]FLUKA version 2021.2.7

based on Geant4[2] (Agostinelli, 2003; Allison, 2006; Allison, 2015). Some additional cross checks were done using the MCNP6.2 (Werner, 2018) and PHITS[3] (Sato, 2018; Ogawa, 2022) programs. The following transport and production thresholds were used for all simulations except the ones using Geant4 (for which the *ShieldingM* physics list with a minimum range cut of 0.010 mm was used):

- 1 keV for everything except
- 10^{-5} eV for neutrons
- 10 keV for photons
- 100 keV for electrons
- 10^{-5} eV for electron and muon (anti-) neutrinos

The carbon density was taken to be 1.86 g/cm^3, while for the tungsten density 19.3 g/cm^3 was used in the simulations. A gaussian width of 1 mm was taken for the 800 MeV proton beam.

Figure 6.5 shows the energy deposited in the tungsten and carbon spheres per primary proton, estimated using FLUKA2021 and MARS15. The agreement between the results obtained with the two programs is remarkably good, especially for the tungsten design. A peak energy deposition of 30 MeV/proton is found for the tungsten design, while the energy deposition for the carbon design peaks at about 6.5 MeV/proton. About 20 kW of power is deposited in the tungsten spheres, while the power deposited in the carbon spheres is about 15 kW.

Figure 6.5. Deposited energy in the tungsten and carbon spheres with FLUKA2021 and MARS15

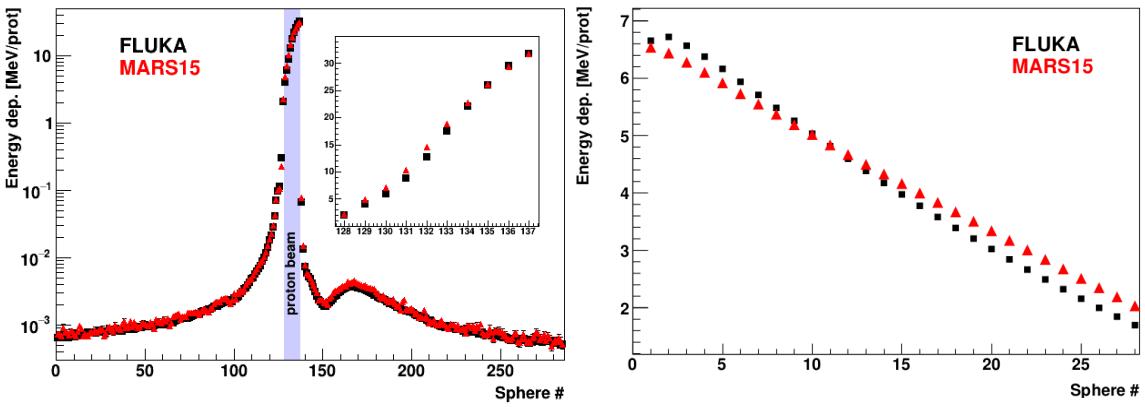

Left: Energy deposition per primary proton for the 285 tungsten spheres estimated with FLUKA2021 and MARS15. The shaded area shows which spheres are directly hit by the proton beam. The inset shows a zoom of the region covered by the proton beam.
Right: Energy deposition for the 28 carbon spheres estimated with FLUKA2021 and MARS15. All 28 spheres are in the trajectory of the proton beam.
Source: FLUKA2021 simulation files can be found at (Müller; 2022), for MARS15 simulations see (Pronskikh; 2022)

[2]Geant4 version 10.07.p02

[3]PHITS version 3.27

An important quantity to characterize the different target designs is the yield of negative muons and pions entering the TS, as these numbers determine the number of muons making it to the aluminum stopping target and eventually undergo a $\mu \rightarrow e$ conversion. These numbers have been studied as a function of momentum using the Geant4-based Mu2e offline framework, FLUKA2021 and MARS15, counting the μ^- and π^- which exit the production solenoid volume towards the TS (i.e. traveling towards the right in Figure 6.3.). Figure 6.6. shows the yield of μ^- and π^- for the tungsten design. The agreement between the codes is again quite good, even if for the π^- yields the MARS15 results are higher above 100 MeV/c momenta. The situation is different for the carbon-based target design, as shown in Figure 6.7. For μ^-, there is a good agreement between MARS15 and Geant4 above 100 MeV/c, while the FLUKA2021 results agree with Geant4 only below about 50 MeV/c. In the case of the π^-, FLUKA2021 and Geant4 agree up to a pion momentum of 100 MeV/c, while the MARS15 results in this region are lower. Above 100 MeV/c, MARS15 and Geant4 are in good agreement, while the FLUKA2021 results are lower. This behavior is not yet fully understood, and further studies are needed. In particular, the models used for muon and pion production in the different radiation transport codes need to be compared in more detail. It should be mentioned that the Mu2e transport solenoid filters out negative particles above 100 MeV/c, therefore the discrepancies seen in the tungsten-based design, which are only above 100 MeV/c, do not affect the studies for Mu2e and Mu2e-II much. This is not the case for the carbon-based design.

Figure 6.6. Particle yields with FLUKA2021, Geant4 and MARS15 for the tungsten design

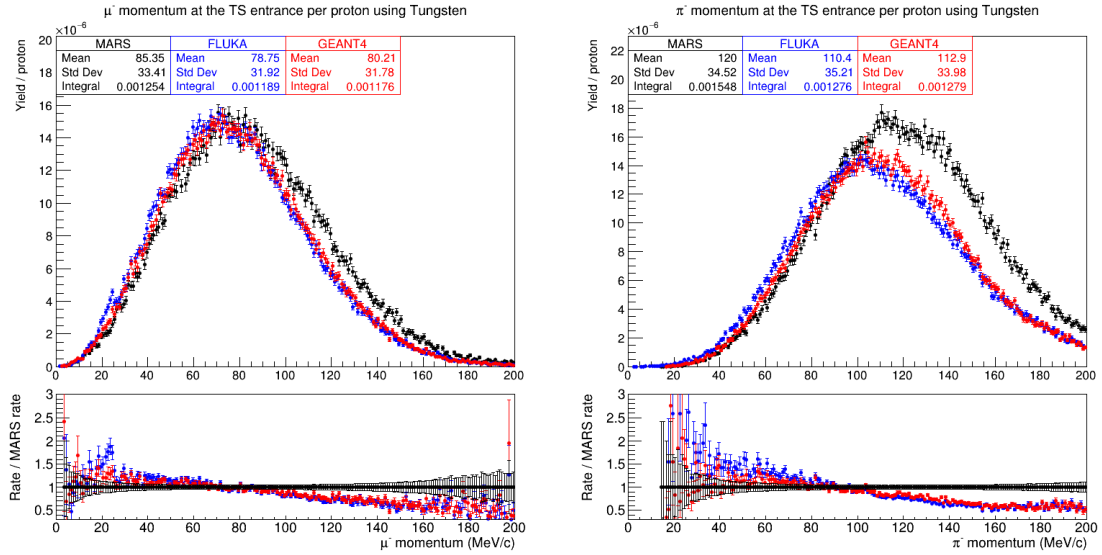

Left: μ^- yield per primary proton as a function of muon momentum for μ^- entering the transport solenoid estimated with FLUKA2021, Geant4 and MARS15.
Right: π^- yield per primary proton as a function of pion momentum for π^- entering the transport solenoid estimated with FLUKA2021, Geant4 and MARS15.
Source: Data points available at (MacKenzie; 2022a), simulation files can be found at (Müller; 2022, Mu2e: 2022, MacKenzie; 2022b, Pronskikh; 2022)

Figure 6.7. Particle yields with FLUKA2021, Geant4 and MARS15 for the carbon design

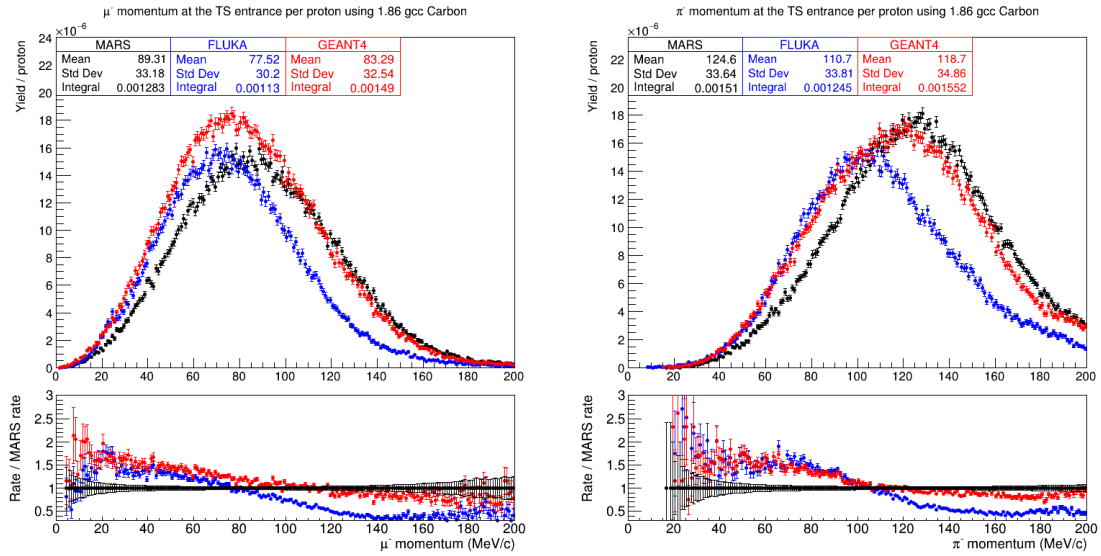

Left: μ^- yield per primary proton as a function of muon momentum for μ^- entering the transport solenoid estimated with FLUKA2021, Geant4 and MARS15.
Right: π^- yield per primary proton as a function of pion momentum for π^- entering the transport solenoid estimated with FLUKA2021, Geant4 and MARS15.
Source: Data points available at (MacKenzie; 2022a), simulation files can be found at (Müller; 2022, Mu2e;2022, MacKenzie; 2022b, Pronskikh; 2022)

6.5. Simulations for the PS1 superconducting magnet coil

Values for radiation damage and energy deposition in the superconducting PS magnet coils have been given for the case of Mu2e using MARS15 in (Pronskikh; 2016). With FLUKA2021, using the particle transport and production thresholds given in Section 1.4., radiation damage and energy deposition values have been estimated for a Mu2e-II beam with protons of 800 MeV energy and a beam power of 100 kW. As an example, Figure 6.8. shows the estimated power density in coil 1 of the production solenoid for the production target design based on tungsten spheres.

Figure 6.8. Power density in coil 1 of the PS, using 800 MeV proton beam with 100 kW beam power for the tungsten design evaluated with FLUKA2021

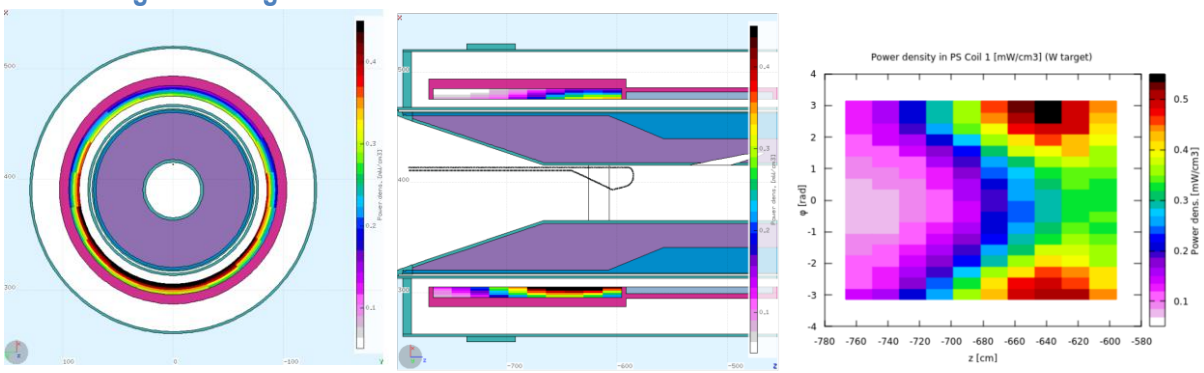

Left: Distribution of power density in the x-y plane in mW/cm^3.
Middle: Distribution of power density in the y-z plane.
Right: Map of power density in φ-z plane.
Source: Simulation files can be found at (Müller; 2022)

Table 6.1 shows the values obtained with FLUKA2021 for deposited energy, DPA ("Displacements-per-Atom") and dose for both the tungsten- and the carbon-based design of the production target. The values for the carbon-based design are 10-15% lower respect to the tungsten-based design. The values in Table 6.1. give important information which can be used as a starting point to understand in which way the current shielding design of the Mu2e experiment can be reused for the higher requirements at a possible Mu2e-II experiment.

Table 6.1. Results for deposited energy, DPA and dose using 800 MeV proton beam with 100 kW beam power evaluated with FLUKA2021

	Tungsten-based design	Carbon-based design
Peak energy deposition [GeV/cm^3/POT]:	4.35 x 10^{-9} ± 1.8%	3.74 x 10^{-9} ± 2.4%
Peak power density [mW/cm^3]:	0.544 ± 1.8%	0.468 ± 2.4%
Peak power density [mW/g]:	0.138 ± 1.8%	0.118 ± 2.4%
Peak DPA [DPA/POT] :	8.67 x 10^{-27} ± 1.8%	7.68 x 10^{-27} ± 2.4%
Peak DPA [DPA/yr]:	1 x 10^{-4} ± 1.8%	0.9 x 10^{-4} ± 2.4%
Peak Dose [GeV/g/POT]:	1.10 x 10^{-9} ± 1.8%	0.95 x 10^{-9} ± 2.4%
Peak Dose [MGy/yr]:	2.06 ± 1.8%	1.78 ± 2.4%

Note: The effective Mu2e-II year is taken as 1.5 x 10^7 s, with 7.8 x 10^{14} protons/s for the 800 MeV proton beam with 100 kW beam power.

6.6. DPA comparisons

A comparison of DPA between MARS and FLUKA for the Mu2e-II target designs is not ready yet. Instead, the original Mu2e cylindrical tungsten target design (cylindrical tungsten rod with 16 cm length and 0.315 cm radius) was used with an 800 MeV proton beam to compare DPA results from FLUKA2021 (DPA calculations based on (Fassò; 2011)), MCNP6 (using the DPA cross sections from (Konobeyev; 2019)) and PHITS (DPA calculations according to (Nordlund; 2018)). In addition, all three codes now offer the possibility to calculate DPA estimates in the earlier NRT model by (Norgett; 1975) which neglects effects of athermal recombination. Figure 6.9. shows the comparison for both models with the three codes. It can be seen that the NRT-based

evaluations give results which are by factors 2-3 larger than the ones obtained with the more sophisticated approaches including athermal recombination effects. From this it becomes clear that when comparing results on DPA for different codes, it should be made clear whether the results are obtained including athermal recombination effects or not. Once this is taken into consideration, the three codes show a good agreement. Remaining differences can be attributed to differences in the underlying models and to different values for the displacement energy threshold, for which each code's proposed value was used (90 eV for FLUKA2021, 70 eV for PHITS and MCNP6).

Figure 6.9. DPA comparisons using FLUKA2021, PHITS and MCNP6

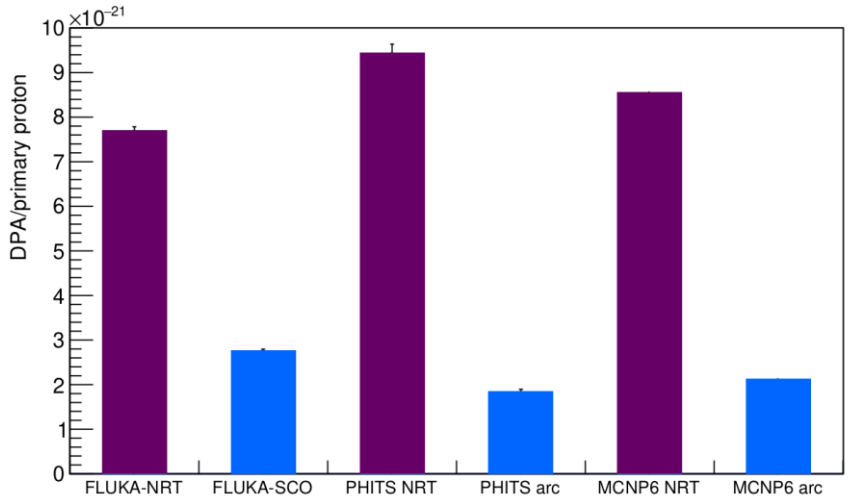

Note: FLUKA-SCO is FLUKA2021's DPA implementation including athermal recombination (arc) effects.
Source: Simulation files can be found at (Ferrari; 2022)

6.7. Summary and Conclusions

We have modeled the pion production target designs for the Mu2e-II experiment using the FLUKA2021, MARS15 and Geant4 radiation transport codes. A good agreement between MARS15 and FLUKA2021 for the energy deposition in the target spheres for both the tungsten- and carbon-based designs is found. For both target designs, we have also studied the μ^- and π^- yields entering the trasportation solenoid with MARS15, FLUKA2021 and Geant4 (which is the default in Mu2e's Offline framework). A fair agreement is found between the different codes, but some local discrepancies in the corresponding momentum spectra are still to be understood and need further inverstigations. Simulation studies of radiation damage, DPA and deposited dose in the superconducting solenoid coils of the production solenoid have been started – this allows one to understand whether the current shielding infrastructure of the Mu2e experiment can be reused. Since a comparison of DPA between MARS and FLUKA for the Mu2e-II target designs is not ready yet, a cross check between FLUKA2021, MCNP6 and PHITS was done using the original Mu2e cylindrical tungsten target design. All three codes show a good agreement both for the NRT-model for DPA and the models using athermal recombination.

6.8. Acknowledgements

V. P.'s work is supported by the Fermi National Accelerator Laboratory, managed and operated by Fermi Research Alliance, LLC under Contract No. DE-AC02-07CH11359 with the U.S. Department of Energy. The U.S. Government retains and the publisher, by

accepting the article for publication, acknowledges that the U.S. Government retains a non-exclusive, paid-up, irrevocable, world-wide license to publish or reproduce the published form of this manuscript, or allow others to do so, for U.S. Government purposes. The work of A. F., S. M. and R. R. was supported by the EU Horizon 2020 Research and Innovation Programme under the Marie-Sklodowska-Curie Grant Agreement No. 101006726 (aMUSE).

6.9. List of references

Cabibbo, N. (1963), "Unitary Symmetry and Leptonic Decays". Physical Review Letters. ***10*** *(12): 531–533, DOI:10.1103/PhysRevLett.10.531*

Kobayashi, M.; Maskawa, T. (1973), "CP-violation in the renormalizable theory of weak interaction". Progress of Theoretical Physics. ***49*** *(2): 652–657, DOI:10.1143/PTP.49.652*

Bartoszek, L. et al. (2015), "Mu2e Technical Design Report", FERMILAB-DESIGN-2014-01 [arXiv:physics.ins-det/1501.05241]

Bertl, W.; Engfer, R.; Hermes, E. et al. (2006), "A search for μ-e conversion in muonic gold", Eur. Phys. J. C **47**, 337–346, DOI:10.1140/epjc/s2006-02582-x

de Gouvêa A. and Vogel P. (2013),"Lepton Flavor and Number Conservation, and Physics Beyond the Standard Model", Progr. Part. Nucl. Phys. 71, 75

Bernstein R. (2019); "The Mu2e Experiment", Front. in Phys. 7, 1

Czarnecki A., Marciano W. J. and Garcia i Tormo X. (2011), "Muon decay in orbit: spectrum of high-energy electrons", Phys. Rev. D84, 013006

Byrum, K. et al. (2022), "Mu2e-II: Muon to electron conversion with PIP-II", Contribution to Snowmass 2021, [arXiv:hep-ex/2203.07569]

Pronskikh, V.; Fang, Y. I.; Lynch, K.; Mueller, S.; Neuffer, D.; Popp, J.; Pushka, D. (2022) "Pion-Production Target for Mu2e-II: Simulation Design and Prototype", International Conference on High Energy Physics ICHEP 2022, July 6-13 2022, Bologna, Italy

Ferrari A., Sala P., Fassò A., and Ranft J. (2005), "FLUKA: a multi-particle transport code", CERN Yellow report 2005-10, 1–406, INFN/TC_05/11, SLAC-R-773

Böhlen T., Cerutti F., Chin M., Fassò A., Ferrari A., Ortega P., Mairani A., Sala P., Smirnov G., and Vlachoudis V.(2014), "The FLUKA Code: Developments and Challenges for High Energy and Medical Applications", Nuclear Data Sheets 120. 211–214

Ferrari A. et al. (2022), "FLUKA: status and perspectives", these proceedings

Sala P. et al. (2022), "The FLUKA group- and point-wise neutron treatment", these proceedings

Vlachoudis, V. (2009), "FLAIR: A Powerful But User Friendly Graphical Interface For FLUKA", Proc. Int. Conf. on Mathematics, Computational Methods & Reactor Physics (M&C 2009), Saratoga Springs, New York

Mokhov N. and Striganov S. (2007), "MARS15 Overview", Fermilab-Conf-07/008-AD

Mokhov N. and James C. (2017), "The MARS code System User's Guide, Version 15 (2016)", Fermilab-FN-1058-APC [Preprint]

Mokhov N. (2022), "MARS15 Code Status and Path Forward", these proceedings

Tropin, I. (2022), "Composite Models in the MARS15 Code", these proceedings

Agostinelli S. et al. (2003), “Geant4 – a simulation toolkit”, Nuclear Instruments and Methods in Physics Research Section A: Accelerators, Spectrometers, Detectors and Associated Equipment 506 no. 3, 250

Allison J. *et al*. (2006), ”Geant4 developments and applications”, *IEEE Transactions on Nuclear Science*, vol. 53, no. 1, pp. 270

Allison J. et al. (2015), “Recent developments in Geant4”, Nuclear Instruments and Methods in Physics Research Section A: Accelerators, Spectrometers, Detectors and Associated Equipment 835, 186

Werner C. J., et al. (2018), "MCNP6.2 Release Notes", Los Alamos National Laboratory, report LA-UR-18-20808

Sato T., Iwamoto Y., Hashimoto S., Ogawa T., Furuta T., Abe S., Kai T., Tsai P., Ratliff H. N., Matsuda N., Iwase H., Shigyo N., Sihver L. and Niita K. (2018), “Features of Particle and Heavy Ion Transport code System (PHITS) version 3.02”, J. Nucl. Sci. Technol. 55, 684-690

Ogawa, T. et al. (2022), “Recent updates and shielding benchmark of PHITS”, these proceedings

Pronskikh V., Glenzinski D., Knoepfel K., Mokhov N., Tschirhart, R. (2016), “A Study Of The Energy Dependence Of Radiation Damage In Superconducting Coils For a Next Generation Mu2e At PIP-II”, Fermilab-Conf-16-095-APC-Em, [arXiv:physics.acc-ph/1612.08931]

Fassò A., Ferrari A., Smirnov G., Sommerer F., Vlachoudis V. (2011), “FLUKA Realistic Modeling of Radiation Induced Damage”, Progr. in Nucl. Science and Techhnology 2, 769

Müller, S. E. (2022), “Particle yield calculations for different target designs at Mu2e-II” [Data set], https://doi.org/10.14278/rodare.2033

Pronskikh, V. (2022), please contact Vitaly Pronskikh <vpronskikh@gmail.com> for details on the MARS15 simulation

MacKenzie M., Mueller S., Pronskikh, V. (2022a), “Particle yields for Mu2e-II target designs” [Data set], https://doi.org/10.5281/zenodo.7451837

MacKenzie M. (2022b), “Particle yields configuration files for Mu2e-II target designs using Mu2e-II Offline in Geant4” [Data set], https://doi.org/10.5281/zenodo.7458378

Mu2e collaboration (2022), "Offline software for the Mu2e experiment", Tag s01_04_00 of the Mu2e Offline Software repository, https://github.com/Mu2e/Offline [github.com]

Konobeyev A. Yu., Fischer U., Simakov S. P. (2019); “Atomic displacement cross-sections for neutron irradiation of materials from Be to Bi calculated using the arc-dpa model”, Nucl. Eng. and Techn. 51, 170

Nordlund K. et al. (2018); “Primary radiation damage: A review of current understanding and models”, Journal of Nucl. Materials 512, 450

Norgett M. J., Robinson M. T., Torrens I. M. (1975); “A proposed method of calculating displacement dose rates”, Nucl. Eng. Des. 33, 50

Ferrari A., Müller S., Rachamin R. (2022), “DPA calculation with FLUKA2021, PHITS and MCNP6” [Data set], https://doi.org/10.14278/rodare.1981

6.10. List of abbreviations and acronyms

(C)LFV	(Charged) Lepton Flavor Violation
PIP-II	Proton Improvement Plan-II
FNAL	Fermi National Accelerator Laboratory (US)
CL	Confidence Level
SM	Standard Model (of Particle Physics)
POT	Protons on Target
PS	Production Solenoid
TS	Transport Solenoid
DPA	Displacements per Atom
NRT	Norgett, Robinson, Torrens